J. Fluid Mech. (1994), *vol.* 273, *pp.* 375–409

Physics of unsteady blunt-fin-induced shock wave/turbulent boundary layer interactions

By LEON BRUSNIAK AND DAVID S. DOLLING
Department of Aerospace Engineering & Engineering Mechanics, The University of Texas at Austin, Austin, TX 78712-1085, USA

(Received 18 August 1993 and in revised form 18 February 1994)

Fluctuating wall-pressure measurements have been made on the centreline upstream of a blunt fin in a Mach 5 turbulent boundary layer. By examining the ensemble-averaged wall-pressure distributions for different separation shock foot positions, it has been shown that local fluctuating wall-pressure measurements are due to a distinct pressure distribution, $\mathscr{P}_i$, which undergoes a stretching and flattening effect as its upstream boundary translates aperiodically between the upstream-influence and separation lines. The locations of the maxima and minima in the wall-pressure standard deviation can be accurately predicted using this distribution, providing quantitative confirmation of the model. This model also explains the observed cross-correlations and ensemble-average measurements within the interaction. Using the $\mathscr{P}_i$ model, wall-pressure signals from under the separated flow region were used to reproduce the position–time history of the separation shock foot. The unsteady behaviour of the primary horseshoe vortex and its relation to the unsteady separation shock is also described. The practical implications are that it may be possible to predict some of the unsteady aspects of the flowfield using mean wall-pressure distributions obtained from either computations or experiments; also, to minimize the fluctuating loads caused by the unsteadiness, flow control methods should focus on reducing the magnitude of the $\mathscr{P}_i$ gradient ($\partial\mathscr{P}_i/\partial x$).

1. Introduction

Flow separation induced by shock wave/turbulent boundary layer interaction can pose significant problems in the design of high-speed transport systems (Holden 1986). One problem is the large fluctuating pressure loads, up to 185 dB or more (Dolling 1993), which can have characteristic frequencies close to the resonant frequencies of vehicle structural components (Pozefsky, Blevins & Laganelli 1989). Additionally, the high heating rates can further threaten the structural integrity of the vehicle. Consequential safeguards to overcome these local structural problems can result in weight penalties which reduce the cost effectiveness and performance of the vehicle.

Shock-induced separation can arise from a variety of sources, including deflected elevons, engine inlets, wing–body junctures, and so on. In the laboratory these are typically modelled using swept and unswept compression ramps, cylinders, and blunt fins. Some of the major features of these flowfields are illustrated in figure 1 for the case of a hemicylindrically blunted fin of leading edge diameter D. In this example, in which the interaction scale is controlled mainly by D, there is a large-scale, three-dimensional, vortical, separated flowfield and, as is typically the case for shock-induced turbulent separation, it is highly unsteady. The unsteadiness is most visibly

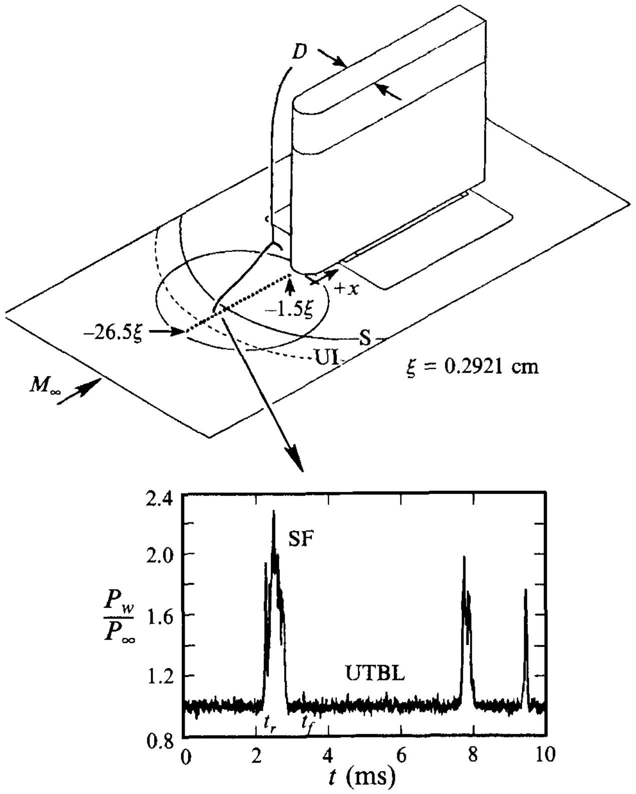

FIGURE 1. Blunt-fin flowfield.

associated with the foot of the separation shock which undergoes aperiodic motion over a streamwise length of order D, between the upstream-influence line (UI) and the separation line (S, deduced using surface tracer flow visualization techniques) (Kussoy *et al.* 1987; Dolling & Brusniak 1991; Dolling & Bogdonoff 1981*b*; Dolling & Smith 1989). The effect of the unsteady shock is clearly visible in the wall-pressure signal of figure 1 which is characterized by a low-amplitude, high-frequency component associated with the incoming undisturbed turbulent boundary layer (UTBL), a high-amplitude, low-frequency component due to the intermittent passage of the shock foot over the transducer, and a high-amplitude, high-frequency component associated with the separated flow (SF) downstream of the shock foot. The bandwidth of the shock-foot-associated low-frequency component is a few hundred Hz to several kHz (Dolling 1993).

In the supersonic regime, Dolling & Bogdonoff (1981*b*) provided some of the first unsteady wall-pressure measurements for unswept fins and determined that pressure fluctuation intensity increased with increasing D/δ. However, only single-point measurements were made so that correlations between various regions under the flowfield could not be investigated. Other, later studies have provided more detailed unsteady pressure measurement results (Narlo 1986; Dolling & Smith 1989; Dolling & Brusniak 1991; Gonsalez & Dolling 1993; P. J. Barnhart 1993 (private communication); Kleifges & Dolling 1993), including effects of leading-edge sweep and sweep of the separation line (S), but only recently has the cause of the unsteadiness been specifically addressed. Dolling & Brusniak (1991) investigated the relationship between wall-pressure fluctuations from under the unsteady shock and separated flow regions. From this exploratory study, it was found that measurements from the region of shock motion correlated strongly with measurements from the location in the separated flow at which the wall-pressure standard deviation distribution attained a local maximum. In addition, the low-frequency component of the energy spectrum at this separated flow station was very similar to the spectrum from the region of shock motion. Also, it was found that shock foot motion correlated with certain pressure variations under the separated flow region and, in particular, that pressure 'pulses' appeared to propagate upstream prior to changes of direction of the separation shock foot. However, a detailed physical explanation of these measurements and correlations was lacking.

Computational studies of swept (Lakshmanan & Tiwari 1993) and unswept (Hung & Buning 1985) blunt-fin-induced separation have also been made. In the latter study, wall-pressure distributions on and off the centreline, and particle paths and pressure and Mach number contours in the plane of symmetry were presented for a Mach 3 flow and compared with experimental data of Dolling, Cosad & Bogdonoff (1979) and Dolling & Bogdonoff (1982). Overall, the comparisons were very good. In both of these computational studies the Reynolds-averaged Navier–Stokes equations were used. Since the random turbulence fluctuations were suppressed in these equations, direct or large-eddy turbulence simulation would be needed to resolve the oscillation (Hung & Buning 1985). In light of this, Hung & Buning concluded that 'since the flow is sensitive to turbulence fluctuation and is inherently unsteady, the most important question is how the flow structure, such as horseshoe vortex and separation line, behaves in a stochastically oscillatory field.' It has since been shown experimentally that the instantaneous separation location occurs just downstream of the separation shock foot and is essentially coincident with the shock foot as it moves, and that the separation line, S, obtained from surface tracer flow visualization indicates the downstream end of the region of shock motion (on the centreline) (Gramann & Dolling 1988). The horseshoe vortex behaviour will be inferred from this present study.

One of the practical goals of research in this area is to reduce the fluctuating pressure loads and high heating rates to levels that the vehicle structure can safely tolerate by using flow control devices and/or creative tailoring of vehicle component shapes. Ideally, computations would be used to evaluate the effectiveness of the various devices and components. However, before this can be done, it is essential that the physics responsible for the unsteadiness be determined and then possibly incorporated into the computational model. Experimentally, however, before even the physics can be determined, the physical source of the fluctuating measurements themselves, be it from a horseshoe vortex or a subsonic separation bubble, must be understood: a simple cross-correlation result is meaningless unless it is understood *why* it has its characteristic shape. Understanding the source of the fluctuating measurements (at a point) requires determining the *global* feature or features of the flowfield which cause the *local* measurements and their resulting properties. It is important to differentiate between the fluctuating *signal* measured at a point and the global, unsteady fluid-flow phenomenon which is occurring, only a local segment of which is being monitored.

The fundamental objective of this research, therefore, is to determine if a correlation exists between pressure fluctuations under the regions of separation shock foot motion, under the incoming undisturbed turbulent boundary layer, and under the separated flow region, and to determine the source of the correlation. The specific tasks

M_∞	4.95
U_∞	766 m s^{-1}
P_o	2.275×10^6 N m^{-2}
T_o	352 K
Re_∞	53.1×10^6 m^{-1}
δ_o	1.50 cm
δ^*	0.66 cm
θ	0.066 cm
Π	0.78
$H(\equiv \delta^*/\theta)$	10.2
Re_θ	3.16×10^4
C_f	7.74×10^{-4}

TABLE 1. Free-stream flow conditions and incoming turbulent-boundary-layer properties.

associated with this objective were: (i) if such a correlation exists, to explain the source of the correlation in terms of global flowfield properties; (ii) to verify the global flowfield property model; and (iii) to examine the implications of the results for flow control methods and flowfield computational methods. The results presented herein explain the findings presented in Dolling & Brusniak (1991) and provide insight into the question of the effect of turbulence fluctuations on the horseshoe vortex raised by Hung & Buning (1985).

2. Experimental program and analysis techniques

2.1. *Wind tunnel and model*

The tests were conducted in the Mach 5 blowdown wind tunnel at the Wind Tunnel Laboratories of the University of Texas at Austin. The test section is 30.48 cm in length, 17.78 cm by 15.24 cm in cross-section, and is essentially a parallel wall extension connected to the nozzle exit. The air is heated by two 420 kW banks of nichrome wire heaters upstream of the settling chamber. The floor of the test section was used as the test surface. Pressure transducers were mounted flush with the surface of a 8.57 cm diameter rotateable plug. The plug (figure 1) had 26 transducer ports available on its centreline at centre-to-centre spacing ξ of 0.2921 cm. Measurements were taken upstream of the model on the centreline.

The model was a hemicylindrically blunted fin of 1.905 cm leading-edge diameter. It had a 2.54 cm wide base extension which fitted into a matching slot in the floor with screws underneath holding the fin in place. The fin had a 1.27 cm streamwise range of travel. Gauge blocks in increments of $0.5\,\xi$ were available for accurate and repeatable fin positioning relative to the transducer array. The overall fin height was 10.16 cm. Based on the criterion of Dolling & Bogdonoff (1981*a*), the height-to-diameter ratio of 5.33 was deemed sufficient for the fin height to be considered 'semi-infinite.'

The nominal free-stream flow conditions and incoming turbulent-boundary-layer properties are shown in table 1. The floor surface temperature was within 8% of the adiabatic value. The boundary-layer characteristics were determined by assuming a constant value of static pressure across it in conjunction with total temperature and Pitot pressure surveys. A least-squares fit to the law of the wall/law of the wake following the procedure of Sun & Childs (1973) was used to obtain the velocity profiles. The turbulent boundary layer developed naturally without the use of trips.

2.2. *Instrumentation and data acquisition*

The fluctuating wall pressures were measured using Kulite miniature pressure transducers (models XCW-062-15A and XCQ-062-50A) installed flush with the instrumentation plug surface. The Kulite transducers are absolute pressure sensors with ranges of 0 to 15 psia (0 to 103.4 kPa) and 0 to 50 psia (0 to 344.7 kPa), respectively. They have a nominal outer case diameter of 0.1626 cm with a pressure-sensitive silicon diaphragm of 0.0711 cm diameter. The diaphragm has a fully active four arm Wheatstone bridge diffused into it and has a natural frequency of about 600 kHz (as quoted by the manufacturer). The actual frequency response is limited to about 50 kHz owing to a perforated screen which protects the diaphragm from damage by dust and other particles. The transducer signals were amplified and then electronically lowpass filtered at 50 kHz before being digitized by LeCroy analog-to-digital (A/D) converters interfaced with a Hewlett-Packard 9000 series computer. The LeCroy data acquisition system has two 12-bit A/D converters which operate on the same clock. Up to four channels per A/D can be sampled simultaneously at a maximum rate of 1 MHz per channel, providing a maximum of eight channels of simultaneously sampled data. The transducers were statically calibrated at least daily, and always after they were repositioned.

2.3. *Test procedure*

Initially, flow visualization studies were conducted to determine the upstream influence and separation line locations so that the pressure transducers could be properly positioned. A variation of the kerosene–lampblack method was used. In this case, diesel fuel was added to reduce the volatility of the mixture. This ensured that the surface streak pattern did not set in its final form until well after steady free-stream flow conditions were established.

Owing to the eight-channel limit, several runs were required to complete some of the four series of tests (A–D). Transducers were located at various stations upstream of the fin root from $x = -0.5\,\xi$ to $-26.5\,\xi$ (refer to figure 1). For analysis A, the reference transducer was held fixed under the incoming undisturbed flow at station $-26.5\,\xi$ and the remaining transducers were positioned downstream of it. The objective was to determine the relationship between the undisturbed flow pressure fluctuations and those at successive downstream stations. For analysis B the reference transducer was located at station $-16.5\,\xi$, for which $\gamma \approx 0.9$ (intermittency, γ, is the fraction of the time that the separation shock foot is upstream of a given point). The objective was to relate the intermittent-region pressure fluctuations to the pressure fluctuations from the regions both upstream and downstream of it and to similarly observe the successive spatial development of the relationship. Analysis C is essentially the same as analysis B, except that the reference transducer was located at station $-18.5\,\xi$ ($\gamma \approx 0.5$) in order to determine if the results depend on the reference transducer location. Finally, a single experiment, D, was carried out to simultaneously monitor the majority of the intermittent region and a local portion under the separated flow for which the intermittent region and separated flow signals were known to be highly correlated. A detailed tabulation of all experiments is provided in Brusniak (1994).

All runs were done at sampling frequencies of either 200 kHz or 500 kHz; the number of records per channel (1 record = 1024 data points) was either 256, 512, or

1024. Note that in analysis A, for the measurement at station $-0.5\,\xi$, the upstream reference transducer was actually at station $-25.5\,\xi$ since only 26 transducer ports were available; however, the results will only be affected by a slight timing difference since the undisturbed flow is still being measured exclusively (unlike the separated flow region, for which measured flowfield properties depend on transducer location).

2.4. *Statistical and time series analysis*

Statistical analysis consisted of calculations of the mean, standard deviation, the third- and fourth-order moments (i.e. skewness and flatness coefficients), and the amplitude probability density distribution of each channel, using the entire data array for each channel. Time series analysis consisted of auto-correlations, cross-correlations, coherence function, and power spectral density estimates (the definition and details of the calculation of these quantities can be found in Bendat & Piersol 1986).

2.5. *Boxcar transformation*

The wall-pressure signals from the intermittent region are characterized by turbulence in the undisturbed and separated boundary layers, as well as a rise and fall in pressure when the shock foot crosses the transducer while moving upstream and downstream (see figure 1). The purpose of the conditional sampling algorithm (a threshold method) is to separate the shock wave component of the intermittent wall-pressure signal from the superimposed turbulent components in order to determine the 'rise' and 'fall' times associated with the shock foot (described below). The intermittent pressure signal is converted into a 'boxcar' form consisting of a series of 0's and 1's in which the 0's correspond to times when the shock foot is downstream of the transducer and 1's to times when it is upstream of the transducer. The time at which the boxcar changes from 0 to 1 is designated the rise time, t_r. Conversely, a boxcar change in value from 1 to 0 is designated the fall time, t_f. These times, indicated in figure 1, are used to determine various properties of the shock wave component of the signal. For example, the percentage of 1's in the boxcar file is the intermittency, γ, of the signal at the given transducer location. Dolling & Brusniak (1989) provide full details of the method.

2.6. *Ensemble averaging*

The purpose of ensemble averaging is to examine what correlation, if any, exists between separation shock foot motion and pressure variations under the incoming undisturbed turbulent boundary layer and under the separated flow region. Four specific shock motion 'events' of interest were the unidirectional shock sweep (in both upstream and downstream directions) and shock changes of direction (downstream-to-upstream motion and vice versa). At the lowest level, an upstream shock sweep over a given station occurs when the boxcar for the station changes from 0 to 1 (t_r), and vice versa for a downstream sweep (t_f). A downstream-to-upstream turnaround over a given transducer occurs when the time interval between a downstream sweep and the following upstream sweep occurs within a small time interval, Δt. An upstream-to-downstream turnaround is defined analogously.

The ensemble-averaging algorithm begins by taking pressure signals sampled simultaneously in the intermittent region and, for example, the separated flow region, searching for an 'event' (such as an upstream sweep) on the intermittent-region channel and examining the signal on the downstream channel at the same sampled time instant. A 'time window' of variable width is set about the specific event of interest (t_r) on the intermittent channel such that information not related to the event is

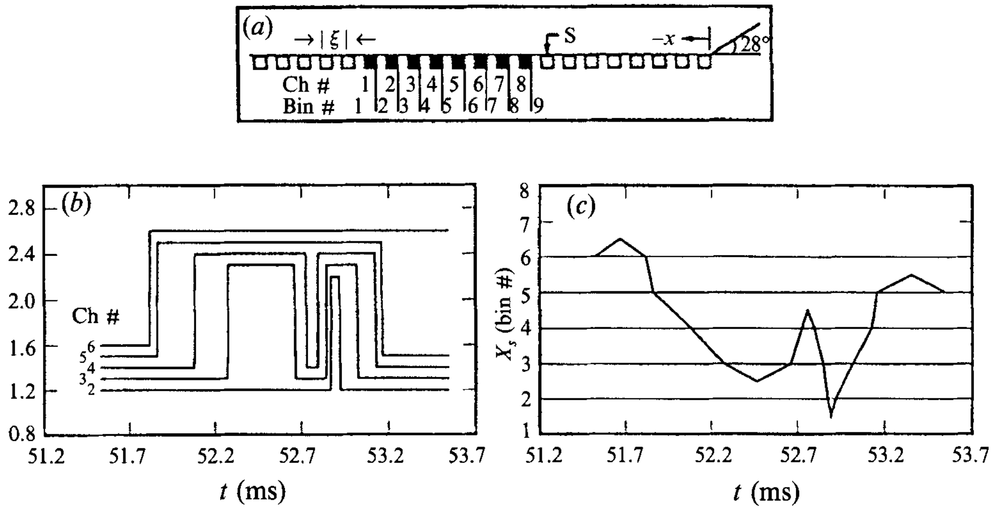

FIGURE 2. Conversion technique for separation shock foot position–time history (from Erengil & Dolling 1993*a*).

excluded, providing a single ensemble for that channel. The same window from the intermittent channel is applied to the separated-flow signal, providing the ensemble for that channel as well. The time axes of the individual ensembles of both channels are then redefined with respect to the rise time, t_r, which is assigned value $\tau = 0$, so that the original timing between channels is retained. That is, time $\tau = 0$ in both ensembles corresponds to the passage of the shock foot over the intermittent-region (reference) transducer. The final step is to take all additional ensembles of each respective channel, 'align' them about each respective $\tau = 0$ reference, and average them to generate the ensemble-averaged result for each channel.

2.7. *Shock foot history,* $X_S(t)$

A detailed discussion on obtaining the separation shock foot position–time history, $X_S(t)$, can be found in Erengil & Dolling (1993*a*), so only a brief description will be given here. $X_S(t)$ is obtained from multichannel wall-pressure measurements on the centreline, where the transducers span the region of shock motion at centre-to-centre spacing ξ (figure 2*a* shows the configuration for a compression ramp, from Erengil & Dolling 1993*a*). The boxcars from each channel can be combined into a nested sequence as shown in the sample of figure 2(*b*). Separate bins are established with boundaries extending from the downstream end of a given transducer to the downstream end of the adjacent transducer. For the present case there are six bins, with bin number 1 being the upstream-most bin, and the rest being numbered consecutively (figure 2*c*).

$X_S(t)$ is obtained from the nested boxcars by linear interpolation between successive rises or successive falls. In cases in which a rise is immediately followed by a fall, which corresponds to an upstream-to-downstream change of direction, the $X_S(t)$ segment between the consecutive rise and fall is obtained by assuming that the shock foot moves at constant speed to the centre of the next bin, changes direction, and then returns at constant speed to the original bin. The same process is applied to downstream-to-upstream changes of direction. Between successively detected rise or fall times there is no information about shock motion owing to the discrete spatial

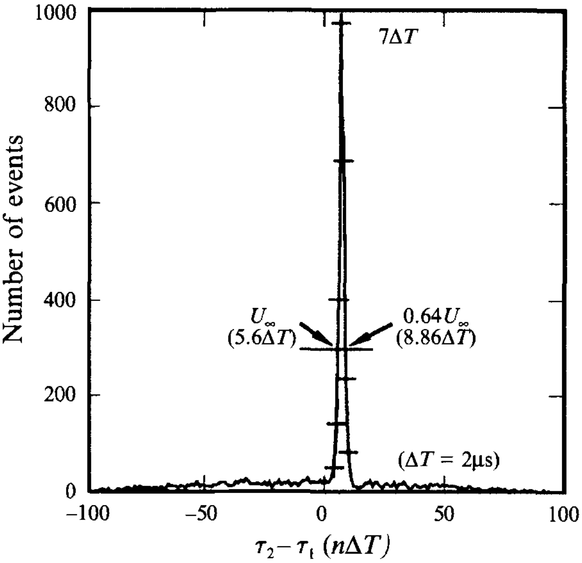

FIGURE 3. Example RSED histogram.

sampling so that frequency decompositions of the $X_S(t)$ history must be viewed with caution owing to this low-pass filtering effect.

2.8. *Random signal event detection (RSED) technique*

In this work, a newly developed technique has been used to detect events in the fluctuating wall-pressure signals which are related to convective phenomena. It is termed the Random Signal Event Detection (RSED) technique, since it can be applied to signals which have a Gaussian distribution. It is a simple algebraic method which requires two streamwise-separated, simultaneously sampled signals. Both arrays of data are subdivided into N contiguous segments of typically 100 to 200 μs in duration. In each successive array segment, the time at which a maximum (or minimum) value occurs in the upstream-most channel is designated τ_1, and the time at which a maximum (minimum) value occurs in the other channel is designated τ_2. The time difference $\tau_2 - \tau_1$ from each parallel segment is added to a histogram array until all segments have been searched. For segments which are 100 μs in duration, all $\tau_2 - \tau_1$ values will fall between -100 and $+100$ μs.

A typical histogram from two undisturbed turbulent-boundary-layer signals is shown in figure 3. In this example the transducers were spaced $3\,\xi$ apart streamwise. As seen, the distribution is dominated by a large spike centred at $7\Delta T$, where $\Delta T = 2$ μs is the sampling time interval, and the spike is defined by about five data points. The bounding values of the spike (where it basically rises above the surrounding 'noise' level) can be understood by considering convection velocities. The maximum convection velocity for a turbulent structure is essentially U_∞, the free-stream velocity. For a $3\,\xi$ spacing this gives a lower bound of about 11 μs (5.6 ΔT) which is used to establish the reference level in the figure. The upper bound in the distribution, as determined from the reference level, is between $8\Delta T$ and $9\Delta T$, corresponding to convection velocities, U_c, of about $0.70U_\infty$ to $0.63U_\infty$, respectively, so that the most probable events convect at velocities in the range $0.63U_\infty \leqslant U_c \leqslant U_\infty$. The most probable time delay is 14 μs ($7\Delta T$), corresponding to $0.81U_\infty$. The standard convection velocity of $0.75U_\infty$ (deduced from cross-correlations) corresponds to 15

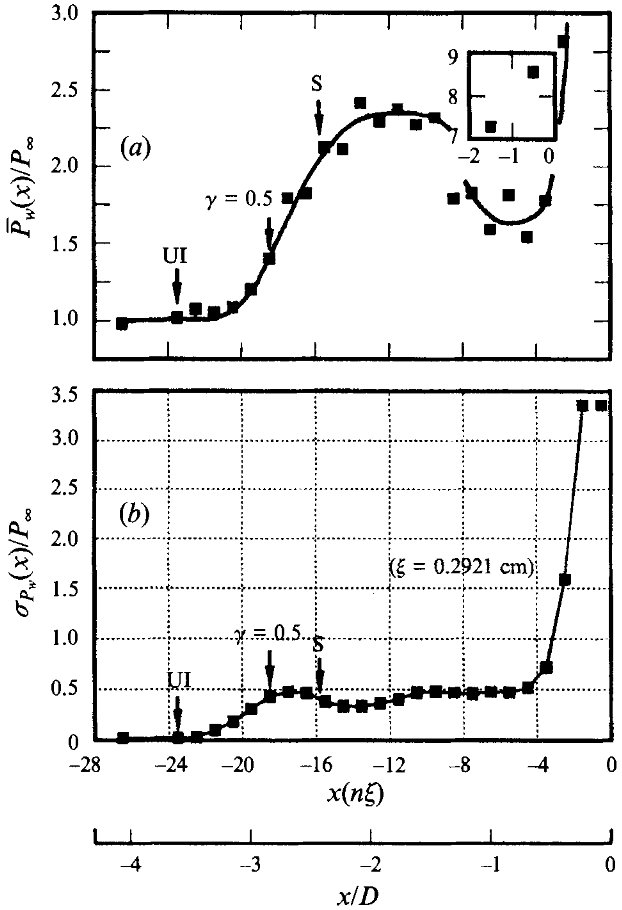

FIGURE 4. (*a*) Mean pressure distribution; (*b*) standard deviation distribution.

μs (7.5 ΔT) which falls between 7ΔT (the most probable value) and 8ΔT in the histogram. The primary significance of this technique is that it can be used to identify 'events' associated with convective features in the undisturbed incoming boundary layer, which can then be correlated with events occurring at other downstream stations (e.g. shock-foot-associated rise and fall times). In addition, this technique provides an independent method for clarifying and confirming some of the cross-correlation and ensemble-average results presented in this study.

3. Discussion of results

3.1. *General flowfield features*

Figure 4(*a*) shows the mean pressure distribution on the centreline upstream of the fin root (the solid line has been added to aid in seeing the variations and is not a least-squares fit to the data). The spatial dimension, x, is in multiples of ξ, since the wall-pressure measurements were all taken at distinct multiples of ξ. Physically, it would be most appropriate to normalize x by fin thickness, D, but for non-integer multiples of D the spatial units would then be several digits in length, making it more cumbersome for discussion. However, for reference, such a scale is shown underneath the ξ scale. The initial increase above the undisturbed pressure level occurs at about

$-23.5\,\xi$, and continues to a maximum value near $-13.5\,\xi$. The distribution is relatively flat from $-13.5\,\xi$ to $-9.5\,\xi$, then decreases rapidly at first ($-8.5\,\xi$), and then more gradually, until approximately $-3.5\,\xi$. The pressure rises rapidly near $-3.5\,\xi$; beyond this it is difficult to resolve owing to this steep gradient. It is probable that the stations at $-1.5\,\xi$ and $-0.5\,\xi$ bracket a local maximum in the distribution, where the $-0.5\,\xi$ station is on the decreasing portion. This is supported by the presence of a local maximum in other studies (see figure 2 of Dolling & Bogdonoff 1981*a*).

The initial increase in $\bar{P}_w(x)$ is due to the increasing contribution to the fluctuating wall-pressure signals of the higher pressure levels downstream of the unsteady separation shock foot. The upstream-most extent of the shock foot motion near $-23.5\,\xi$ is referred to as the upstream-influence location (UI), and the downstream-most extent of the motion is indicated in figure 4(*a*) by S at $-15.8\,\xi$, the separation location obtained using surface tracer techniques. The $\gamma = 0.5$ location is also indicated in the figure. As seen, the data have some scatter. This is due largely to the difficulties of measuring mean pressures in the 0 to 14 kPa range using transducers having a 0 to 103 kPa or 0 to 345 kPa range. The wide range is necessary to ensure high-frequency response; lower-range transducers have more flexible diaphragms with a lower useable frequency range.

Figure 4(*b*) shows the wall-pressure standard deviation distribution. It is characterized by an increase beginning at UI, a maximum at $-17.5\,\xi$, a decrease to a minimum at $-13.5\,\xi$ and an increase to a plateau region which begins at about $-9.5\,\xi$. Near $-3.5\,\xi$, $\sigma_{P_w}(x)$ increases rapidly to an apparent local maximum between stations $-1.5\,\xi$ and $-0.5\,\xi$. In contrast with the $\bar{P}_w(x)$ distribution, the $\sigma_{P_w}(x)$ distribution has little scatter since the mean value has been subtracted from the data for the calculation.

3.2. *Cross-correlation results: analysis A*

The cross-correlation results from analysis A are summarized in figure 5. Recall that for this case, the reference transducer was fixed under the undisturbed turbulent boundary layer at station $-26.5\,\xi$ and simultaneous measurements were made at successive stations downstream of it. Seven characteristic cross-correlations are evident, with representative results being shown in the figure. (Note that the ranges in figure 5 (similarly for figures 7 and 9) over which each curve is representative are indicated in the figure; also shown (in parentheses) are the stations at which each curve was obtained.) The most obvious result is that a correlation *does* exist between signals from under the incoming undisturbed boundary-layer flow and both the intermittent and separated flow regions. Each cross-correlation tends to have one, or both, of two modes: a broad mode inferred to be due to low-frequency components in the measured signals and a sharp mode inferred to be due to high-frequency contributions. The sharp mode (indicated by the arrows for curves 1–4) is evident in all curves and occurs at progressively later time delay. The broad mode is evident in curves 2, 4, 6, and 7 and has a maximum R_{xy} value which alternates between negative and positive (note that the broad mode exists in 17 of the 22 stations downstream of station $-22.5\,\xi$). By defining a ‘transition’ point as the location at which the character of the broad mode changes, it is evident that stations $-14.5\,\xi/-11.5\,\xi$ and $-3.5\,\xi$ fit this definition; the former separates regions of well-defined cross-correlations spanning approximately $6\,\xi$ to $7\,\xi$ in range (i.e. from $-21.5\,\xi$ to $-15.5\,\xi$, and from $-10.5\,\xi$ to $-4.5\,\xi$) with the latter at the downstream end of such a region. By regarding curve 6 as initiating a new region following transition point $-3.5\,\xi$, then an additional transition point would apparently occur downstream

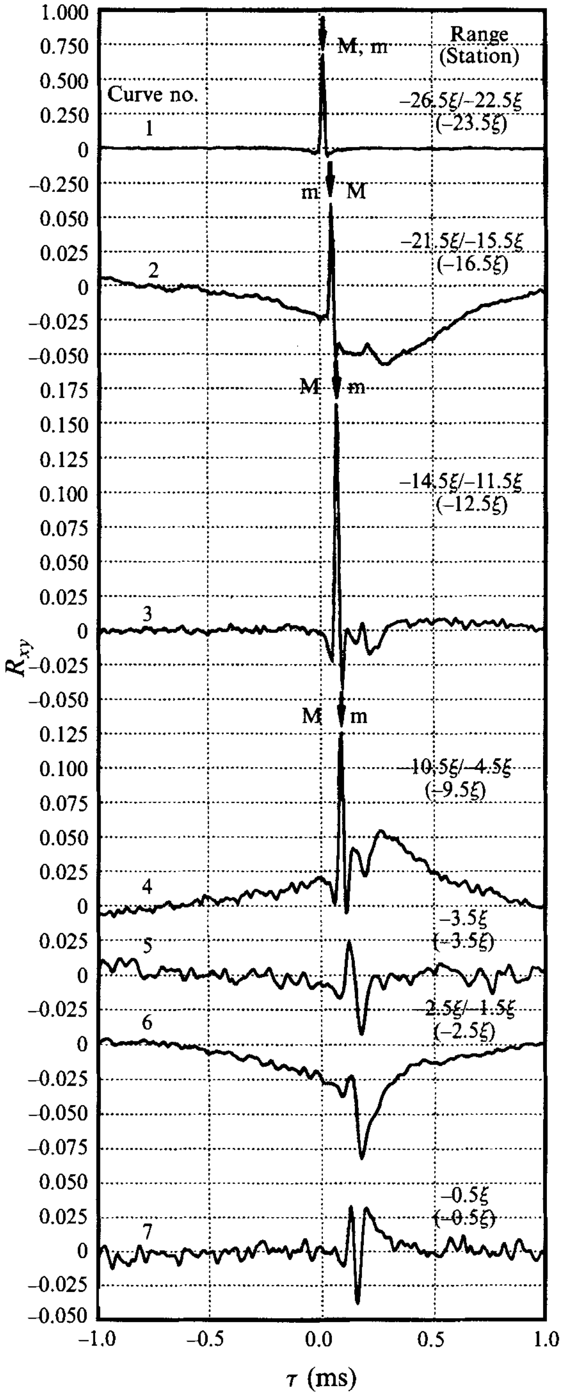

FIGURE 5. Analysis A cross-correlations.

of station $-1.5\,\xi$, perhaps between curves 6 and 7 at about $-1.0\,\xi$. These transition points are indicated in table 2. The existence of a broad mode in the cross-correlation, especially as represented by curve 4, suggests that a low-frequency component must

R_{xy}:A	$-14.5\xi/-11.5\xi$, -3.5ξ, -1.0ξ
R_{xy}:B	$-13.5\xi-4.0\xi$, -1.0ξ
R_{xy}:C	$-14.5\xi-4.0\xi$, -1.0ξ
Ensemble average:B	$-13.5\xi-3.5\xi$, -1.0ξ
Ensemble average:C	$-14.5\xi-4.0\xi$, -1.0ξ

TABLE 2. 'Transition' points.

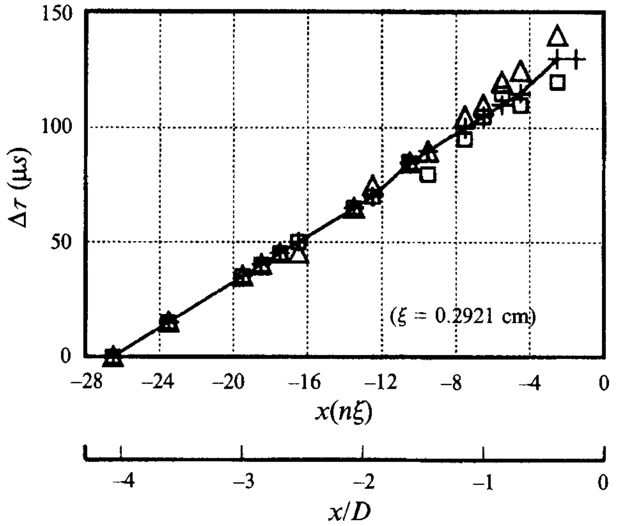

FIGURE 6. Time delay, analysis A: +——+ R_{xy} ; □, RSED maximum point criterion; △, RSED minimum point criterion.

exist in the incoming undisturbed boundary-layer signal. This feature will be further investigated in § 3.5.

It is evident from curves 1–5 that the sharp mode always has a positive value of R_{xy} and positive time delay up to station $-3.5\,\xi$. The data from station $-23.5\,\xi$ (curve 1) are dominated by undisturbed boundary-layer flow so that the sharp mode is due to the downstream convection of turbulent eddies in the boundary layer. The time delay of the maximum corresponds to a convection velocity of $0.75U_\infty$, which agrees with the typical broadband convection velocity for an undisturbed turbulent boundary layer. The fact that the sharp mode is present from stations $-22.5\,\xi$ to $-3.5\,\xi$ and that it occurs at progressively later time delay is evidence of the convection of eddies in the incoming boundary layer into the separated shear layer and through the interaction, to at least station $-3.5\,\xi$. As a consequence, the sharp mode can be regarded as a distinct perturbation on the broad-mode portion of the cross-correlation so that both modes can be considered separately.

The results of time delay calculations using the RSED technique on the same data set are indicated in figure 5 as either 'M' (maximum point criterion) or 'm' (minimum point criterion) and they agree very well with the sharp mode peaks. In addition, figure 6 shows the time delay as a function of location from both the cross-correlation and RSED results. The close agreement in the figure shows that the RSED technique is capable of tracking events in the incoming undisturbed flow as they enter and pass through the interaction.

3.3. *Cross-correlation results: analysis C*

The results from analysis C are summarized in figure 7. Recall that for this case, the reference transducer was located at station $-18.5\,\xi$ (the middle of the intermittent region, $\gamma = 0.5$). Just as for analysis A, analysis C yields seven characteristic cross-correlations, demonstrating that a correlation does exist between the intermittent region and the incoming undisturbed flow (already seen in analysis A) and between the intermittent and the separated flow regions. The curves are generally bimodal in character, having a broad and sharp mode. A broad mode (which dominates most of the curves) is evident and has a maximum R_{xy} value which alternates between negative and positive (in the downstream direction). Curve 3 has broad-mode features characteristic of curves 2 and 4 and is therefore a transition point. Station $-4.0\,\xi$ is also considered as a transition point (curve 5 is actually from just downstream of this point; a transducer located at $-4.0\,\xi$ would most probably produce a cross-correlation resembling both curves 4 and 5), and station $-1.0\,\xi$ is another transition point. These stations are indicated in table 2. In order to see the variation of the broad mode with position, the R_{xy} maximum value for the broad mode as a function of location is shown in figure 8. As seen, the transition points correspond to the locations at which the cross-correlation coefficient changes sign. They are therefore related to changes in character of the low-frequency component of the fluctuating pressures with position.

The sharp mode is clearly distinguishable up to station $-11.5\,\xi$ and apparently continues to be evident as a distortion on the broad mode up to approximately $-4.5\,\xi$ (figure 7). The RSED results tend to agree with this (see arrows, curve 4). In figure 5 the sharp mode (due to turbulent-boundary-layer convection) was clearly distinguishable for a larger distance since the reference station transducer measured the undisturbed incoming flow exclusively so that the convecting structures were more readily detected. The fact that the sharp mode is evident from stations $-26.5\,\xi$ to approximately $-4.5\,\xi$ and that it occurs at progressively later time delay indicates that it is due to the convection of structures in the incoming boundary later into and through the interaction. The sharp mode is not always of positive value (see curve 4) as was the case in figure 5. Since the pressure fluctuations due to the incoming undisturbed flow are much smaller in both duration and magnitude than the large fluctuations downstream of the shock foot, the cross-correlations will be strongly dominated by the broad mode. Although this is the case, the timing of the sharp mode agrees with the RSED calculations. In light of these results the sharp mode is again seen to be a distinct perturbation on the broad mode. Analysis B produced essentially the same results as analysis C; the transition points are also shown in table 2.

3.4. *Ensemble-average results*

The ensemble-average results from analysis C, figure 9, show seven characteristic pressure signatures associated with upstream and downstream shock foot sweeps over the reference transducer at station $-18.5\,\xi$. The solid horizontal lines in the figure are the mean pressure levels of the entire signal at the given stations. For the upstream sweep case, the incoming undisturbed flow result (curve 1(u)) is characterized by an S-shaped signature of small amplitude and short duration, just to the left of $\tau = 0$ (i.e. the variation occurs at the upstream station *before* the shock foot has crossed

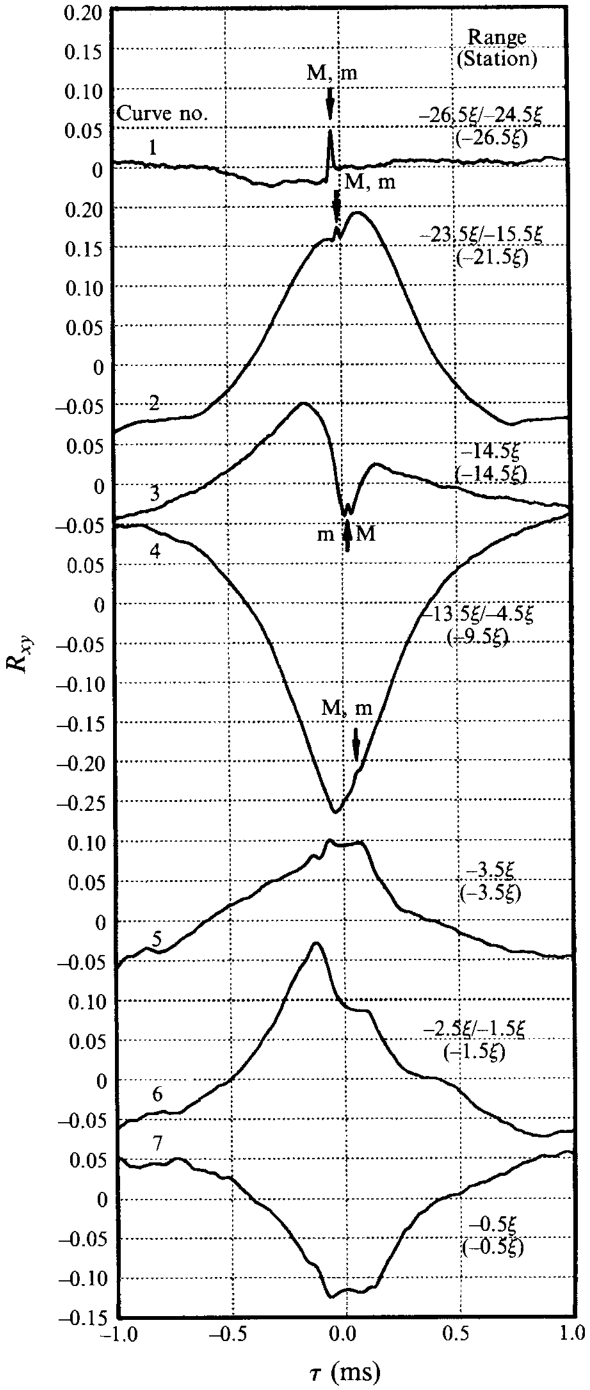

FIGURE 7. Analysis C cross-correlations.

the reference transducer). Ensemble averages from the intermittent region (curve 2(u)) have a low level corresponding to undisturbed flow followed by a rapid rise to higher levels due to passage of the shock foot over the pressure transducer. Although this broad signature dwarfs the undisturbed flow signature, the latter is still evident

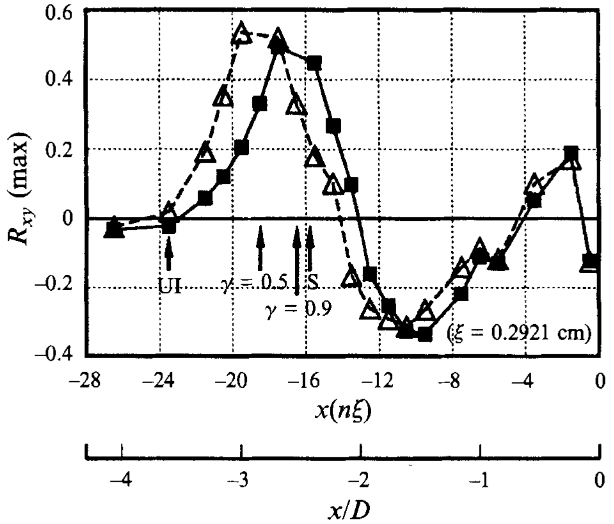

FIGURE 8. Cross-correlation broad mode (R_{xy} maximum) distributions: ■, analysis B ($\gamma = 0.9$); △, analysis C ($\gamma = 0.5$).

near $\tau = 0$. The character of the ensemble averages changes rapidly at about station $-14.5\,\xi$ to the peaked signature shown in curve 3(u). The peaked character is strongest at this station; proceeding downstream the rising portion to the immediate left of the peak increases in level such that the peak becomes no longer discernible by about station $-11.5\,\xi$. From there to station $-4.5\,\xi$ the ensemble averages are characterized by a broad drop in pressure levels (curve 4(u)). Station $-3.5\,\xi$ (curve 5(u)), which is characterized by a low level and then a rise in pressure, is apparently the beginning of a change in character from falling levels (curve 4(u)) to the broad rising pressure characteristic of the station immediately downstream of it (station $-2.5\,\xi$, curve 6(u)). There is a change in character once more between stations $-1.5\,\xi$ and $-0.5\,\xi$ to one of a broad falling pressure (curve 7(u)). This change likely occurs between these two stations since no 'combination' of trends is evident. As such, stations $-1.0\,\xi$ and $-4.0\,\xi$ are designated as transition points. Station $-14.5\,\xi$ is also so designated since it is the station at which its peak is first clear. These points are indicated in table 2.

The sharp signature, S, seen in curve 1(u) is also evident in curve 2(u) but, as seen, is dwarfed by the large pressure increase across the shock foot. Its passage through the interaction is still evident in curves 3(u) and 4(u) as a small perturbation just to the right of $\tau = 0$ but is difficult to discern owing to the presence of other similar perturbations in the ensemble averages. The RSED results indicate where the peaks corresponding to boundary-layer convective phenomenon should occur and help in discerning which of the sharp variations in the ensemble averages are associated with boundary-layer convection and which are not.

For the downstream sweep case, the above discussions hold analogously. The primary difference is that the results, for the most part, are mirror-images about $\tau = 0$ of the upstream sweep results: the curve 1(d) sharp signature is now a 'backward S' shape, the curve 2(d) signature exhibits a broad *fall* in pressure as the shock foot crosses to downstream of the pressure transducer; in curve 3(d) the pressure levels to the left of the peak now *fall* and instead the pressure levels to the *right* of the peak increase in level. The broad changes in curves 4(d), 6(d), and 7(d)

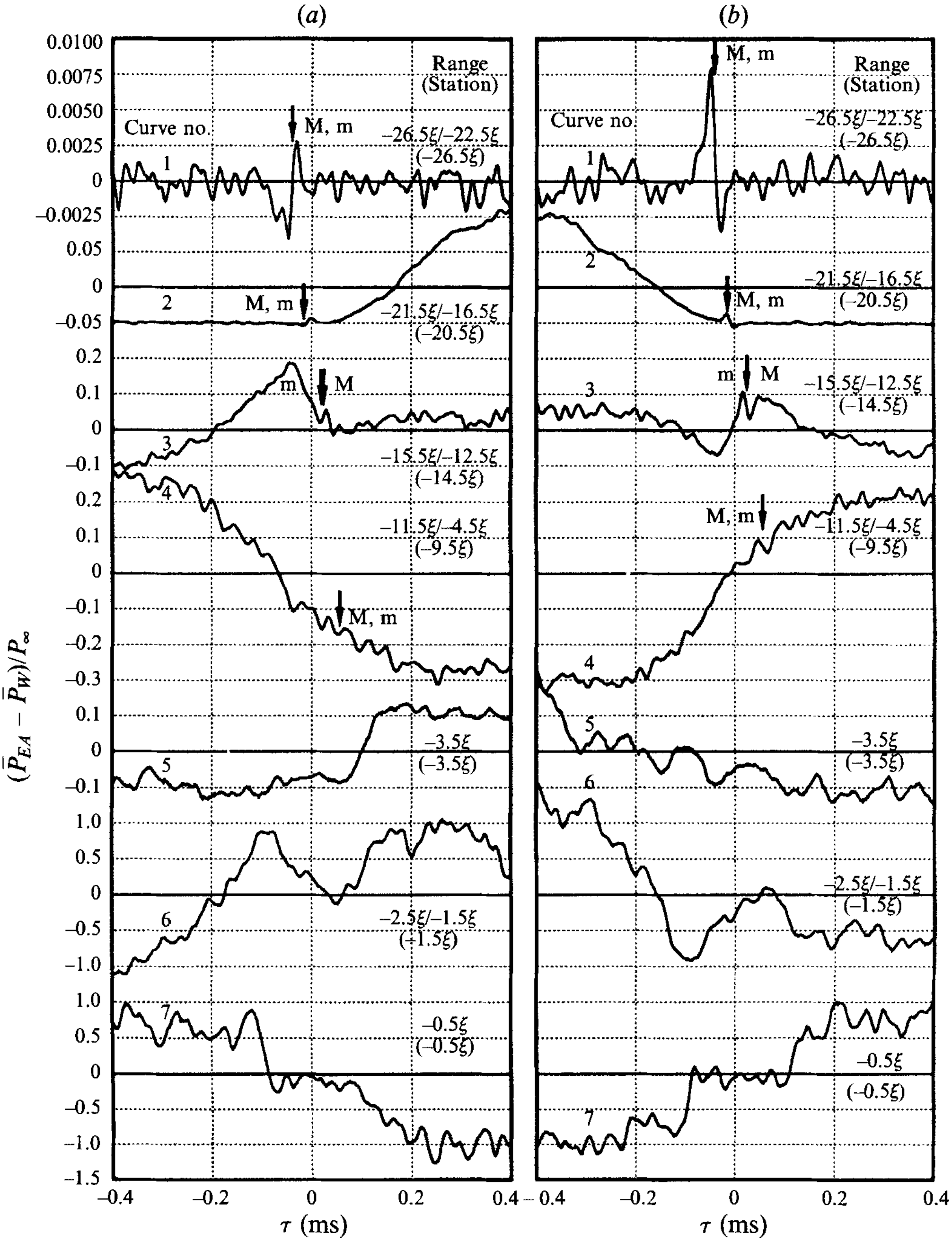

FIGURE 9. (*a*) Analysis C upstream (u) sweep ensemble averages; (*b*) analysis C downstream (d) sweep ensemble averages.

are now opposite in nature to the upstream sweep case; curve 5(d) is apparently from just downstream of a transition point.

The analysis B results are essentially the same as for analysis C, and the transition points are also included in table 2.

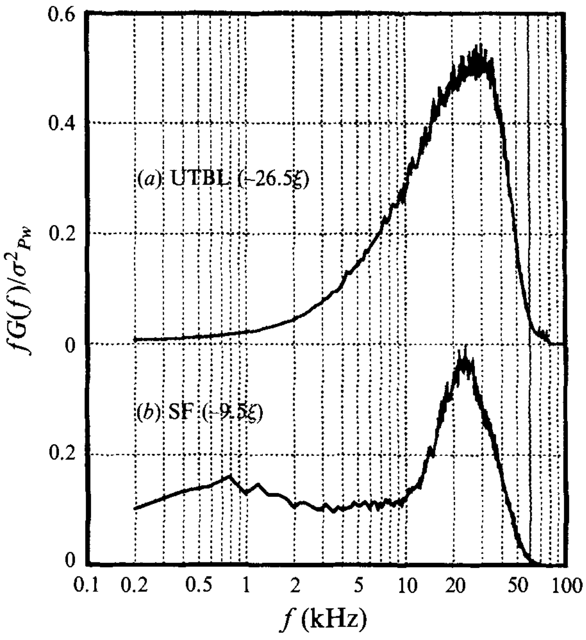

FIGURE 10. Power spectra from under: (*a*) undisturbed incoming turbulent boundary layer; (*b*) separated flow region.

3.5. *Digital filtering results*

As discussed earlier (§3.2), the broad mode in curve 4 of figure 5 suggests that a low-frequency component exists in the incoming undisturbed boundary-layer signal. To investigate this aspect further, power spectra from the stations used to obtain the curve are shown in figure 10 (the complete set of power spectra is shown in Brusniak 1994). The vertical axis is plotted as $fG(f)/\sigma^2_{p_w}$ since in this form the area under each curve will be unity. Since $\sigma^2_{p_w}$ for the undisturbed boundary layer is underestimated, the normalization is not entirely accurate; however, it is retained for purposes of discussion. As seen in figure 10(*b*) (station $-9.5\,\xi$), a significant band of energy below about 4 kHz exists, with the largest concentration being centred at about 0.8 kHz. In curve 4 of figure 5, the broad mode extends from approximately $\tau = -0.5$ to 1.0 ms, which corresponds to 0.67 kHz. This value falls clearly within the low-frequency band of figure 10(*b*) and is close to the large energy concentration centred at 0.8 kHz. In figure 10(*a*), from the undisturbed flow ($-26.5\,\xi$), there is no clear low-frequency band below 4 kHz. In fact, the spectrum is quite flat in this region; however, it is not zero in value.

In order to demonstrate that the broad mode in curve 4 of figure 5 is related to a low-frequency component in the undisturbed flow, the signal was highpass filtered at a cut-off frequency (f_c) of 4 kHz using an FIR non-recursive digital filter. The unfiltered result is shown in figure 11(*a*). The filtered result (figure 11*b*) shows that the broad mode has been completely removed from the cross-correlation. It is not necessarily surprising that this occurs, in light of the relationship between cross-correlations and power spectra, but it does illustrate the point. Note that the remaining sharp mode extends from approximately $\tau = 0$ to 0.2 ms, implying that it is associated with frequencies higher than about 5 kHz.

In order to investigate the undisturbed flow low-frequency phenomenon further,

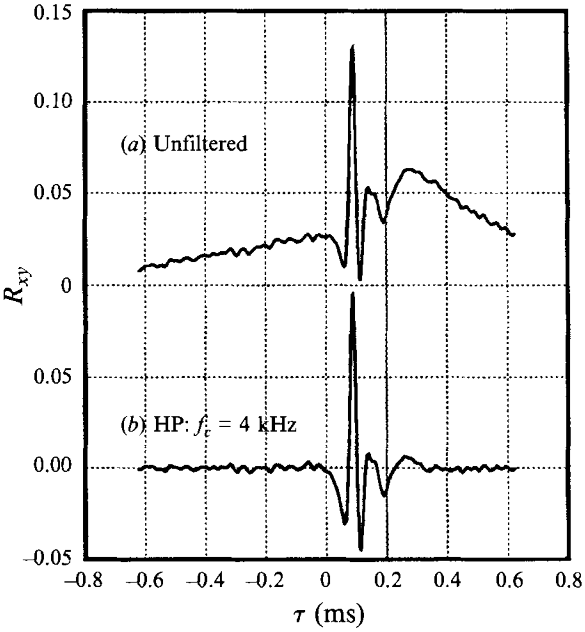

FIGURE 11. Digital filtering of incoming flow/separated region cross-correlation.

lowpass digital filtering was used in conjunction with ensemble averaging. This was done by filtering the entire undisturbed flow data string *before* ensemble averaging. Results were obtained using various f_c values in order to determine if a low frequency (broad signature) – which correlates with separation shock motion – could be detected. Figure 12(*a*) shows the unfiltered ensemble average for the case of shock foot upstream sweep. By decreasing f_c to lower and lower values so that more and more of the high-frequency content in the signal is removed, the sharp S-shaped signature in the upstream sweep ensemble average (solid line, figure 12*a*) was gradually suppressed and then suddenly disappeared for $f_c = 10$ kHz, leaving an ensemble average characterized by a broad dip in pressure values (solid line, figure 12*b*) at just around $\tau = -0.1$ ms. The dip is small, but certainly physical, since its shape reverses for a change in shock direction of motion (see figure 12*e* discussion, below). This low-frequency signature is suppressed in magnitude with further decreases in f_c, but remains evident. For the downstream sweep case, as f_c was decreased the sharp 'backward S' signature (figure 12*d*) was increasingly suppressed. In this case, at $f_c = 10$ kHz, the ensemble average is characterized by a broad hump in pressure values. This low-frequency signature also becomes increasingly suppressed for further decreases in f_c, but from the sequence shown in the figure it is still evident. There is not as obvious an abrupt change in character when f_c is decreased from 20 to 10 kHz for the downstream sweep case as occurred in the upstream sweep case. This occurs since the low-frequency hump (downstream sweep case, figure 12*e*) is similar in shape to the unfiltered case (a 'sharp hump', figure 12*d*), whereas, for the upstream sweep, it is easy to contrast the unfiltered sharp signature (figure 12*a*) with the resultant low-frequency signature dip of figure 12(*b*) (i.e. opposite characters). For $f_c = 4$ kHz (figures 12*c* and 12*f*), there is an apparent gradual decreasing level for the upstream sweep case and, more so, of a gradual increasing level for the downstream sweep case from $\tau = -0.4$ to 0.4 ms. A similar small effect was observed in the compression ramp experiments

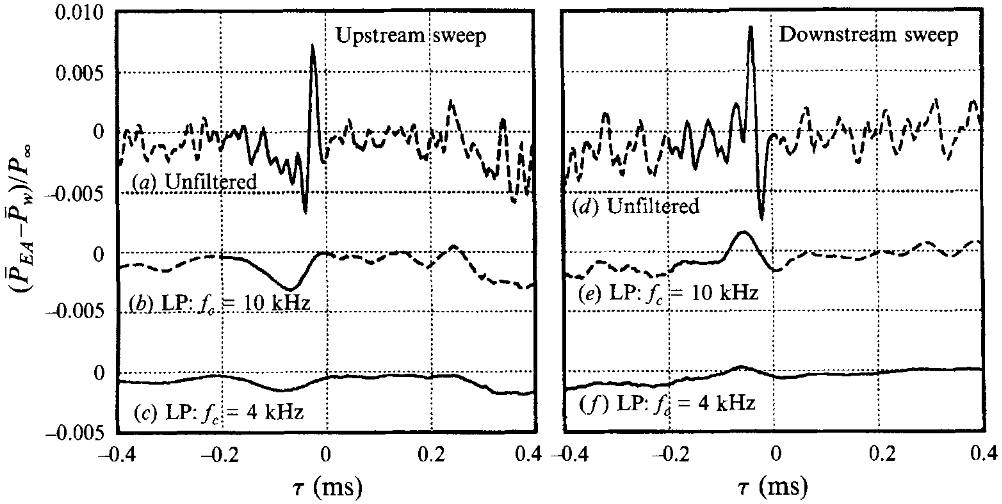

FIGURE 12. Digital filtering of undisturbed flow ensemble average.

of McClure (1992) where the undisturbed flow measurements were made in the flow using a fluctuating pressure Pitot probe. It was observed that a gradual decrease in Pitot pressure occurred during shock upstream sweeps and that an increase in pressure occurred during downstream sweeps. The total change (increase or decrease) was typically 25% of the fluctuating Pitot pressure standard deviation and spanned at least 1 ms in time. For the present results the changes in pressure are less than roughly 8% of the wall-pressure standard deviation value, but they also span at least 1 ms in time.

In summary, a low-frequency component in the undisturbed flow signal is responsible for the broad mode of the station $-9.5\,\xi$ cross-correlation of analysis A (curve 4, figure 5). This component is due to frequencies less than about 4 kHz. From the ensemble-average results it was seen that low-frequency (broad) pressure signatures exist which correlate with shock motion and are a function of shock direction of motion.

4. Interpretation of mean pressure and standard deviation distributions, ensemble averages, and cross-correlations

As discussed in § 1, it is necessary to determine the *global* flowfield behaviour in order to explain *local* (point) measurements and the behaviour of the two-point correlations and ensemble averages. A global flowfield representation which attempts to synthesize the mean pressure and standard deviation distributions, and is able to show that the ensemble averages and cross-correlations are the result of a single global effect will be presented in this section.

4.1. *Global flowfield property ($\mathscr{P}_i$) hypothesis*

The mean wall-pressure distribution in figure 4(*a*) gives a ‘zeroth-order’ global description of the centreline pressure field. This description, however, does not account for the unsteady aspect of the flowfield. A global description which provides a first-order inclusion of the unsteadiness is the ensemble-averaged pressure distribution at time $\tau = 0$. This time corresponds to the separation shock foot being located directly over the given intermittent-region pressure transducer and therefore provides

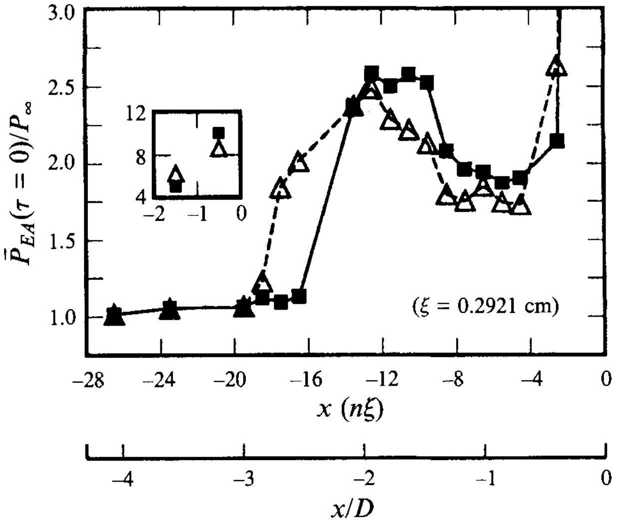

FIGURE 13. Shock-foot-fixed ensemble-averaged wall-pressure distributions: ■, analysis B ($\gamma = 0.9$); △, analysis C ($\gamma = 0.5$).

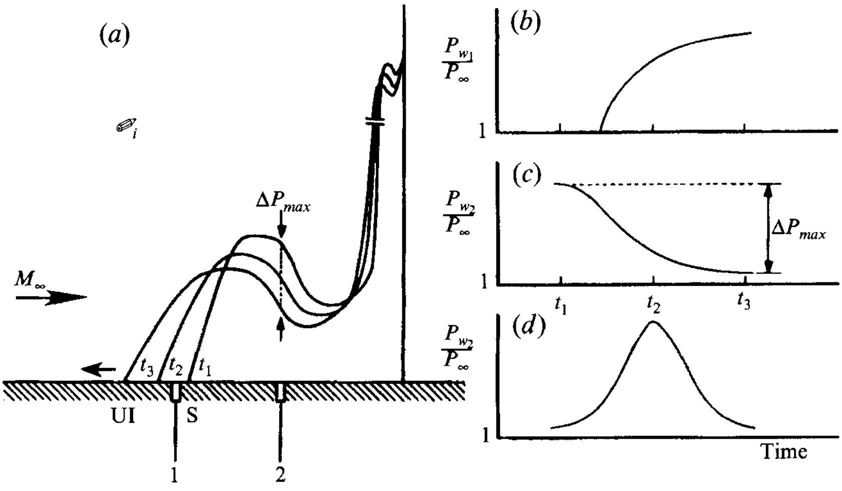

FIGURE 14. (a) $\mathscr{P}_i$ distribution; pressure–time variation for shock foot upstream sweep at (b) station 1, (c) station 2; (d) pressure–time variation at station 2 for shock foot downstream-to-upstream turnaround.

the ensemble-averaged pressure distribution as a function of x for the shock foot 'fixed' at the given station; this distribution can be obtained for shock motion in the upstream and downstream directions.

The ensemble-averaged wall-pressure distribution $[\bar{P}_{EA}(x)]$ for the upstream sweep case with the shock foot fixed at the downstream end of the intermittent region ($\gamma = 0.9$, station $-16.5\,\xi$) is shown in figure 13. Both sweep cases provide basically the same result (for clarity, only the upstream sweep result is shown) and essentially resemble the mean pressure distribution of figure 4(*a*), except that the initial pressure rise begins at the shock foot location, station $-16.5\,\xi$. The ensemble-average wall-pressure distribution for the shock foot fixed at station $-18.5\,\xi$ ($\gamma = 0.5$) is also shown in the figure and is also similar in shape to the mean wall-pressure distribution and

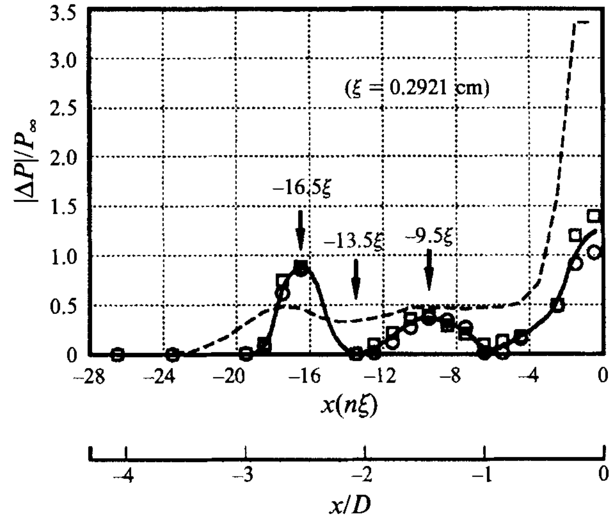

FIGURE 15. Predicted standard deviation distribution based on: □, shock foot upstream sweep; ○, shock foot downstream sweep; ——, actual $\sigma_{P_w}(x)$ distribution.

$\gamma = 0.9$ distribution. The difference is that the $\gamma = 0.5$ distribution has been 'stretched' further and the pressure levels are lower ('flatter').

Figure 13 illustrates that, although a distortion of the $\bar{P}_{EA}(x)$ distributions occurs for the two shock-foot-fixed cases, the distributions are essentially similar and resemble the mean wall-pressure distribution. These results lead to the hypothesis that the local wall-pressure (point) measurements and correlations are due to the global effects of an 'instantaneous' wall-pressure distribution, $\mathscr{P}_i$, corresponding to any given $\bar{P}_{EA}(x)$ distribution, the upstream end of which translates aperiodically and undergoes a stretching and flattening effect which is a function of where the shock foot is located in the intermittent region. Therefore, local pressure variations measured at a given point will be due largely to the range of pressures associated with a local segment of the $\mathscr{P}_i$ distribution which likewise translates aperiodically over the measurement point.

The hypothesis is illustrated in figure 14(*a*) for a hypothetical shock foot upstream sweep from S to UI. $\mathscr{P}_i$ is shown at three instants in time and, as sketched, $\mathscr{P}_i$ stretches and flattens during the sweep. Figures 14(*b*) and 14(*c*) show the resulting pressure variations sensed at the wall at the two corresponding stations shown in figure 14(*a*). The pressure at station 1 is initially at the undisturbed free-stream level since the shock foot is still downstream of it; the pressure then rises rapidly owing to the passage of the leading edge of $\mathscr{P}_i$ over station 1. At station 2, the pressure is initially at its highest level since the leading edge of $\mathscr{P}_i$ is at S (t_1). As time progresses and the shock foot moves upstream, $\mathscr{P}_i$ both translates and flattens, so that the pressure at station 2 decreases with time. At time t_3 the pressure at station 2 is at its lowest level since the leading edge of $\mathscr{P}_i$ is at UI. The total change in pressure sensed at station 2 (ΔP_{max}) is the difference of the pressure levels for times t_1 and t_3.

4.2. *Pressure standard deviation estimation from* $\mathscr{P}_i$

If the $\mathscr{P}_i$ model is correct, it should be possible to predict properties such as the wall-pressure standard deviation distribution. Again consider station 2 of figure 14(*a*): as the shock foot translates back and forth, locally the wall pressure will increase

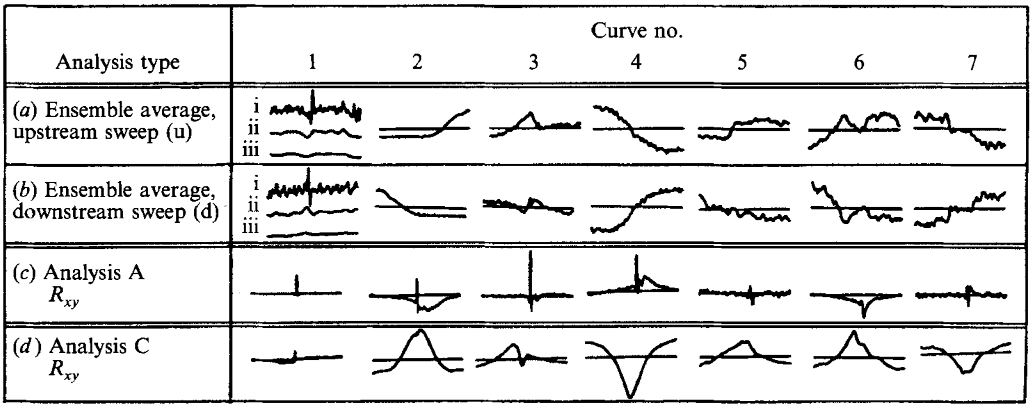

FIGURE 16. Ensemble-average and cross-correlation results summary.

and decrease, the magnitude of the change depending on the local segment of $\mathscr{P}_i$. Now, σ_{P_w} is essentially a measure of the mean difference between the elements of the discrete data series and its mean value. For this case, an approximation to σ_{P_w} at any given point is taken to be the absolute value of the pressure change at the given station ($|\Delta P|$) which occurs when the leading edge of $\mathscr{P}_i$ is moved from one end of the intermittent region to the other. This corresponds to $|\Delta P_{\max}|$ of figures 14(*a*) and 14(*c*). The result of shifting the leading edge of $\mathscr{P}_i$ from station $-16.5\,\xi$ to $-18.5\,\xi$ (or from $-18.5\,\xi$ to $-16.5\,\xi$), where $\gamma = 0.9$ and 0.5, respectively, is shown in figure 15, where the solid line has been sketched as an aid to the eye. These γ values represent the maximum shift in $\mathscr{P}_i$ [i.e. $\bar{P}_{EA}(x)$] which could be obtained from the experimental data sets. As seen, maximum values occur at about stations $-16.5\,\xi$, $-9.5\,\xi$ and near $-1.0\,\xi$, and minimum values occur at about station $-13.5\,\xi$ and near $-6.5\,\xi$, in close agreement with the maxima and minima in the original $\sigma_{P_w}(x)$ distribution which is also shown in the figure. As in figure 4(*b*), little scatter is seen in the $|\Delta P|$ data. This simple result provides the first quantitative evidence in support of the $\mathscr{P}_i$ model.

As seen, the $|\Delta P|$ distribution overpredicted the local $\sigma_{P_w}(x)$ measurements from about $-17.5\,\xi$ to $-14.5\,\xi$. The reason for this is that the shock foot by definition spends 50% of the total time upstream (or downstream) of the $\gamma = 0.5$ station, whereas it only spends 10% of the time *downstream* of the $\gamma = 0.9$ station; consequently, the calculated $|\Delta P|$ values are representative of only a small fraction of the entire pressure–time histories obtained between $-17.5\,\xi$ and $-14.5\,\xi$ so that the $|\Delta P|$ values are being overestimated. The underprediction for stations $-13.5\,\xi$ to $-1.5\,\xi$ is likely due to a decreasing correlation between the upstream end of $\mathscr{P}_i$ and the downstream part of $\mathscr{P}_i$ (i.e. disturbances associated with shock foot motion will be strongest near the shock, but weaker further away from the shock) or to the use of only two $\bar{P}_{EA}(x)$ distributions for the calculation. If a series of $\mathscr{P}_i$ distributions spanning 'S' to UI were available, then the shock foot intermittency distribution could be used in order to increase the accuracy of the $\sigma_{P_w}(x)$ estimation.

4.3. *Ensemble averages in terms of $\mathscr{P}_i$*

Figure 16 summarizes the ensemble average and cross-correlation results using miniatures from figures 5, 7, 9, and 12. Each row, labelled (*a*)–(*d*) corresponds to the specified analysis set. Since there are basically seven distinct curves from each analysis set, they are indicated by the 'curve numbers' at the top of figure 16. For this section, only the ensemble-average results in rows (*a*) and (*b*) will be addressed. In the description of figure 16 that follows the upstream and downstream sweep cases are distinguished by either a (u) or (d), respectively, affixed to the end of the curve number. Also, the curve 1 results in rows (*a*) and (*b*) show the three characteristic pressure signatures found from the digital filtering analysis results of figure 12, and are distinguished as being of character i, ii, or iii, with the appropriate (u) or (d) notation.

From the $\mathscr{P}_i$ model, the ensemble-average sweep signatures should correspond to motion of local segments of $\mathscr{P}_i$. Consider the upstream sweep case first (figure 16, row (*a*)). As seen in the curve 2(u) ensemble average, when the shock foot moves upstream over a given point, the pressure increases from its undisturbed value. Now, when the front edge of $\mathscr{P}_i$ translates upstream, the pressure at a point on the surface just ahead of the upstream edge of $\mathscr{P}_i$ will initially see an undisturbed level, followed by an increase (figure 14*b*), just as seen in the ensemble-average result. Next, ensemble-average curve 3(u) has a peak which is characteristically evident in the region $-14.5\,\xi$ to $-11.5\,\xi$. For a point in this region, as $\mathscr{P}_i$ moves upstream, the local maximum in $\mathscr{P}_i$ will cause the pressure at the point to increase, then decrease, just as in the ensemble average. The peak is less pronounced in this figure than for the analysis B results (not shown), probably owing to the stretching and flattening effect. By continuing this approach, it is clear that $\mathscr{P}_i$ will produce the decreasing pressure levels in curve 4(u), the increasing levels in curve 6(u), and the decreasing levels in curve 7(u). These last two features again imply that a secondary maximum in $\bar{P}_w(x)$ exists near the fin root, but the most striking evidence of this is the fact that, in addition to the overall broad increase in pressure in curve 6(u), a local peak in curve 6(u) (indicative of this local maximum) is clearly visible, analogous to the peak in curve 3(u). (Note also from the $\bar{P}_{EA}(x)$ distributions (figure 13, inset) that as the shock foot position is changed from the 0.9 intermittency to the 0.5 intermittency location, the pressure value at station $-1.5\,\xi$ increases and the pressure value at station $-0.5\,\xi$ decreases. This is entirely consistent with the expectation that a local maximum exists in the $\bar{P}_w(x)$ distribution between these stations.) In addition, curve 6(u) suggests that this local peak is part of an overall increasing level (see $\mathscr{P}_i$ sketch, figure 14*a*). The transition point figure, curve 5(u), is of small magnitude and has the beginnings of characteristics of curve 6(u) and is indicative of the passage of a local minimum in $\mathscr{P}_i$.

For the downstream sweep case, the above discussion holds analogously. In particular, for a point between stations $-21.5\,\xi$ and $-15.5\,\xi$, as $\mathscr{P}_i$ shifts downstream the pressure at the point will decrease and level off at the undisturbed value, just as seen in the ensemble-average result, curve 2(d) of row (*b*). The relationship between $\mathscr{P}_i$ and the remaining downstream sweep curves agrees as well. Curve 5(d), which is of small magnitude, does not quite show a minimum in $\mathscr{P}_i$, but this is likely due to weak competing influences of the curve 4 and curve 6 pressure variations. However, its small magnitude of variation, compared to the magnitude of the pressure decrease at the $-2.5\,\xi$ station just downstream of it, agrees with its being at a local minimum in $\mathscr{P}_i$.

By considering the Dolling & Brusniak (1991) pressure 'pulses' in light of these results, it is clear that they are due to the $\mathscr{P}_i$ distribution. For a downstream-to-upstream shock foot turnaround, the peak in the separated-region ensemble averages occurs since, as the shock foot moves downstream the separated-region transducers detect the falling portion of $\mathscr{P}_i$ (i.e. the portion of $\mathscr{P}_i$ between about $-12\,\xi$ and $-8\,\xi$ as in the $\gamma = 0.5$ case in figure 13) so that the measured pressure *increases* with time; then, as the shock foot changes direction (to upstream), the measured pressure *decreases*, giving the peak 'pulse' result (see figure 14*d*). The minimum

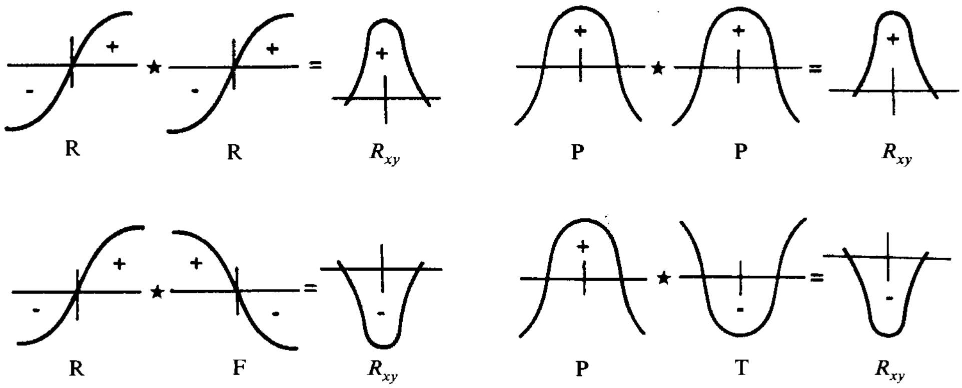

FIGURE 17. Qualitative model signal cross-correlation results.

occurs for upstream-to-downstream changes of direction since, as the shock foot moves upstream, the separated-region transducers measure falling levels, followed by increasing levels as the shock foot changes direction of motion. The 'pulses' therefore are not convective phenomena. The upstream 'pulse' convection suggested by Dolling & Brusniak (1991) can now be interpreted correctly to mean that pressures induced by the vortex motion (and the resultant changes in measured pressure) precede changes in direction of the separation shock foot (i.e. that the separated flow is responsible for the shock foot unsteadiness).

4.4. *Cross-correlations in terms of* $\mathscr{P}_i$

Before considering the cross-correlation results, it will be helpful to discuss some qualitative features of cross-correlation calculations. First, several model signals are given in figure 17. Included are signals characterized by rising levels (R), falling levels (F), a rising-falling or peak (P) signal, and a falling-rising or trough (T) signal. As seen, when the maximum cross-correlation value is calculated for the rise-rise (R-R) combination, the integral will be of an integrand which is always positive (for τ not equal to 0) since, for time $\tau < 0$ both signals are negative and for $\tau > 0$ both signals are positive; the cross-correlation maximum will be of positive value, as suggested in the figure. The same result is obtained for F-F, P-P and T-T combinations. Along similar lines, it is clear that R-F, F-R, P-T and T-P combinations will result in a negative maximum cross-correlation value. Of course, the overall shape of the entire cross-correlation for any of the above model combinations can differ, but here the maximum value is what is of interest. With these qualitative cross-correlation relationships in mind, the detailed cross-correlation results can now be related to the ensemble-average characteristic signatures, which in turn stem from $\mathscr{P}_i$.

4.5. *Analysis A discussion*

The analysis A cross-correlation results are summarized in row (*c*) of figure 16. Consider first the non-transition-point regions from the ensemble-average results (rows (*a*) and (*b*), curves 1, 2, 4, 6, and 7). As seen, the ensemble averages are generally of a broad signature type with superimposed sharp mode variations; the broad mode results will be addressed first. Cross-correlation curve 2 (row (*c*)), between the incoming undisturbed flow and an intermittent-region station, is characterized by a broad mode of overall negative value. From the qualitative models this would suggest an F-R or an R-F relationship between the two regions. From the curve 2(u) upstream sweep ensemble-average results the intermittent region is characterized by a R-type signature and the incoming flow signature 1-iii(u) is apparently an F-type signature, in agreement with the expected relationship (F-R). For downstream sweeps the F-type behaviour in the intermittent region and the R-type behaviour in the incoming flow likewise agree (R-F). The fact that the relationship suggested by the ensemble averages can be seen in the cross-correlation adds validity to the apparent existence of the subtle broad mode measured at the surface under the incoming undisturbed flow (curves 1-iii(u) and 1-iii(d) of rows (*a*) and (*b*)). Next, cross-correlation curve 4 has a broad mode of overall positive value. This suggests that like-behaviour occurs in both signals (R-R and/or F-F). This is indeed the case: both the incoming and separated-region upstream sweep ensemble-average signatures (curves 1 and 4, row (*a*)) are of F-type; both are of R-type for the downstream sweep case. Continuing this approach, it is seen that the F-R (upstream sweep)and R-F (downstream sweep) combinations lead to the overall negative character in cross-correlation curve 6 and that the F-F (upstream sweep) and R-R (downstream sweep) combinations in the ensemble averages lead to the overall positive character in cross-correlation curve 7. As seen, the curves 6 and 7 cross-correlation broad modes are more complex in overall shape than the cases already discussed; the variations may be more closely related to the 1-i(u)/1-i(d) or 1-ii(u)/1-ii(d) characteristic signatures correlating with the local maximum in $\mathscr{P}_i$ near the fin root. The important point is that the overall maximum values in the cross-correlations agree with the qualitative models. The transition point in cross-correlation curve 3 has no broad mode since locally $\sigma_{P_w}(x)$ is at a minimum so that the broad mode contribution to the overall $\sigma_{P_w}(x)$ value is at a minimum (locally, the flattened portion of $\mathscr{P}_i$ is translating over this region, resulting in the $\sigma_{P_w}(x)$ minimum values); the transition point in cross-correlation curve 5 has a positive maximum and a negative maximum, suggesting that the station $-3.5\,\xi$ data contains information from the stations just upstream and just downstream of it, similar to what was seen in the curves 5(u) and 5(d) of the ensemble averages.

In cross-correlation curves 1–4 (row (*c*)) the sharp mode always has a positive-valued maximum. This can be attributed to the convection of a given signature shape through the interaction where the same signal signature shape is detected at successive downstream stations (see curves 1-i(u) and 1-i(d) and the sharp signatures in the curves 2 and 3 ensemble averages which result in a P-P or T-T behaviour). It is not clear if this behaviour persists beyond station $-4.5\,\xi$ (this station might represent the downstream-most extent of boundary-layer convection). For the transition point of cross-correlation curve 3 only the sharp mode is present. This is due to the fact that this station is at a local minimum in the $\sigma_{P_w}(x)$ distribution, where the broad mode fluctuations are also at a local minimum, so that the sharp mode is primarily evident.

4.6. *Analysis C discussion*

For the cross-correlation results of analysis C (row (*d*) of figure 16), the discussion follows essentially the same lines as for analysis A, starting with the broad modes of the non-transition points. Recall that the reference transducer was located in the intermittent region (i.e. curves 2(u) and 2(d)). Cross-correlation curve 1 of analysis C is the opposite of curve 2 of analysis A since for the latter the undisturbed flow transducer was the reference while for the former the intermittent-region transducer was the reference. The same ensemble-average relationship between the measurement stations (R-F, F-R) of course holds for the analysis C result. For cross-correlation curves 2 and 6 (row (*d*)), the positive maxima occur since the ensemble averages (e.g. curves 2(u)/6(u) and 2(d)/6(d)) are of an R-R or F-F nature. Further, the negative maxima of cross-correlation curves 4 and 7 can be related to the R-F/F-R behaviour in curves 2(u)/4(u) and 2(d)/4(d), and curves 2(u)/7(u) and 2(d)/7(d) of the ensemble averages. Curves 6 and 7 of row (*d*) are also of a more complicated nature, as in analysis A.

The sharp-mode behaviour in analysis C is due to a P-P/T-T relationship as in analysis A. The sharp mode is evident in curves 1–4 of row (*d*) (weakly in 2) but is not as well defined as before. This is probably due to the fact that for analysis A the reference transducer predominantly detects sharp mode fluctuations whereas, for case C, it is dominated by the broad mode.

The transition point indicated by cross-correlation curve 3 (row (*d*)) has characteristics similar to those of curves 2 and 4. The 'indented' portion for $\tau \approx 0$ is the beginning of a rapid transition to the shape in curve 4. Also, curve 5 is similar to curve 6, suggesting that curve 5 represents the initial influence of the $\mathscr{P}_i$ effect seen in curve 6.

4.7. *Additional remarks*

By referring to table 2 and figure 8 it is now clear that the transition points from cross-correlation analyses B and C correspond to the stations centred near $-14.0\,\xi$, $-4.0\,\xi$ and $-1.0\,\xi$, for which the cross-correlation coefficient changes sign and also for which the ensemble averages record the passage of a local maximum or minimum in $\mathscr{P}_i$. Further, they are associated with the stations at which little change in pressure occurs when the leading edge of $\mathscr{P}_i$ translates (near regions where $\partial\mathscr{P}_i/\partial x$ is small; see figure 13). An additional test series was done with pairs of transducers (at $1\,\xi$ spacing) positioned throughout the centreline flowfield. The cross-correlation results agree entirely with the $\mathscr{P}_i$ model. A complete discussion is provided in Brusniak (1994).

5. Validation of flowfield model through prediction of shock foot motion

In the preceding sections it was seen that the ensemble averages had a broad and a sharp signature; similarly, the cross-correlations had a broad and a sharp mode. The sharp signature of the ensemble averages and sharp mode of the cross-correlations were attributed to the incoming turbulent boundary layer convecting through the interaction. From the ensemble-averaged wall-pressure distributions at $\tau = 0$ the hypothesis that a 'self-similar' pressure distribution, $\mathscr{P}_i$, was responsible for the measured flowfield properties downstream of UI was proposed and investigated. From the model, the $\sigma_{P_w}(x)$ shape was predicted accurately, the broad signatures in the ensemble averages were related logically to local segments of $\mathscr{P}_i$, and the broad modes in the cross-correlations were explained via $\mathscr{P}_i$ using qualitative cross-correlation models.

The ensemble averages used so far have not distinguished between different types of shock sweep motions, which include short sweeps which occur over only 1 transducer before the shock turns around, and long sweeps which can occur successively over several transducers. All of these motions are included in the ensemble-average results, so that no distinction exists between low-frequency, large-amplitude oscillations and high-frequency, small-amplitude 'jitter' motion of the shock foot. The question then is whether the $\mathscr{P}_i$ model is accurate only in a time-averaged sense or if it is representative at each instant in time as well. One way to approach this question is to ask the following: if the wall pressure at a given point under the separated flow is due to an instantaneous, 'self-similar' $\mathscr{P}_i$ distribution, can the separated-region

	$\overline{P}_{EA}$ (kPa, u/s sweep) at station x				$\overline{P}_{EA}$ (kPa, d/s sweep) at station x			
$X_S(-n\xi)$	-8.5ξ	-9.5ξ	-10.5ξ	-11.5ξ	-8.5ξ	-9.5ξ	-10.5ξ	-11.5ξ
19.5	7.591	8.791	8.970	9.515	7.784	9.267	9.536	9.791
18.5	8.046	9.556	9.942	10.253	8.391	10.094	10.377	10.487
17.5	8.563	10.322	10.811	10.914	9.184	11.025	11.163	10.873
16.5	9.342	11.301	11.528	11.211	9.922	11.728	11.597	11.039
r^2	0.9916	0.9980	0.9978	0.9844	0.9986	0.9987	0.9907	0.9609

TABLE 3. Calibration values for $x_S(t)$ prediction.

pressure values at each instant in time be used to *predict* the instantaneous location of the separation shock foot? This would check whether the separated-region pressure levels correlate with shock foot location in an instantaneous as well as time-averaged sense. The approach is as follows: first, obtain the shock foot time history $[X_S(t)]$ directly, using the intermittent wall-pressure data; second, use the separated-region pressure signals to obtain the predicted shock foot time history $[x_S(t)]$; then, use basic statistical and spectral analyses to compare the two results.

The procedure used to obtain $x_S(t)$ is as follows (the procedure for obtaining $X_S(t)$ was described in §2.7). For this experiment, four transducers were located in the intermittent region from $-16.5\,\xi$ to $-19.5\,\xi$, spanning an intermittency range of 0.9 to 0.25. Although this corresponds to only about 50% of the total range of the shock foot motion in physical space, it encompasses a large range of intermittency values (i.e. most of the shock foot motion could be monitored). The second set of four transducers was located in the separated region from $-8.5\,\xi$ to $-11.5\,\xi$, all well downstream of S. First, ensemble averages for both upstream and downstream sweeps were obtained, from which the separated-region ensemble-averaged pressures at time $\tau = 0$ versus shock foot location were obtained (table 3). Next, for each separated-region station, a least-squares linear curve fit between shock foot location and ensemble-averaged pressure was obtained, with the corresponding r^2 values shown in table 3; by doing this separately for each channel, transducer zero drift effects could be avoided. Finally, $x_S(t)$ at each instant in time was obtained by calculating four x_S values from each of the separated-region pressure–time values using the calibration curves and then averaging the four x_S values to produce a single weighted estimate for $x_S(t)$ at the given time instant. Although the calibration was done for the shock foot range of $-16.5\,\xi$ to $-19.5\,\xi$ only, the extrapolated values of $x_S(t)$ were retained in the prediction.

Figure 18 shows simultaneous samples of both $X_S(t)$ and the $x_S(t)$ shock foot history obtained using the above approach. The $X_S(t)$ signal displays a low-frequency trace; $x_S(t)$ exhibits both low- and high-frequency variations. From a statistical analysis of $x_S(t)$, the mean location was calculated to be at stations $-18.24\,\xi$ and $-18.77\,\xi$ for the upstream sweep and downstream sweep calibration curves, respectively. This is in close agreement with the station at which the measured value of γ is equal to 0.5, station $-18.5\,\xi$. From the wall-pressure measurements it is known that the intermittent region extends from about $-15.0\,\xi$ to about $-23.5\,\xi$. The $x_S(t)$ result, based on the extrapolated data, predicts an intermittent region extending from $-12.1\,\xi$ to $-24.4\,\xi$ and $-12.0\,\xi$ to $-25.5\,\xi$ for the upstream and downstream sweep cases,

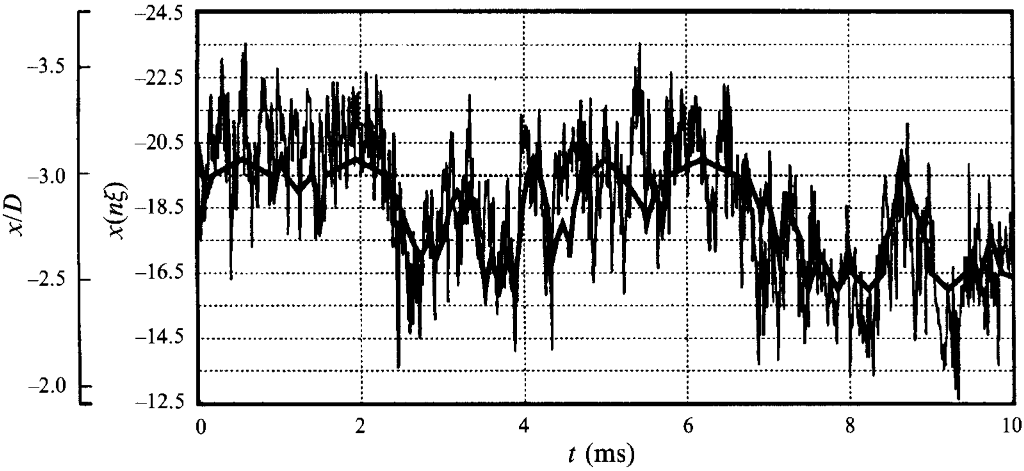

FIGURE 18. Sample shock foot position–time history: ——, actual $[X_S(t)]$; ——, predicted $[x_S(t)]$.

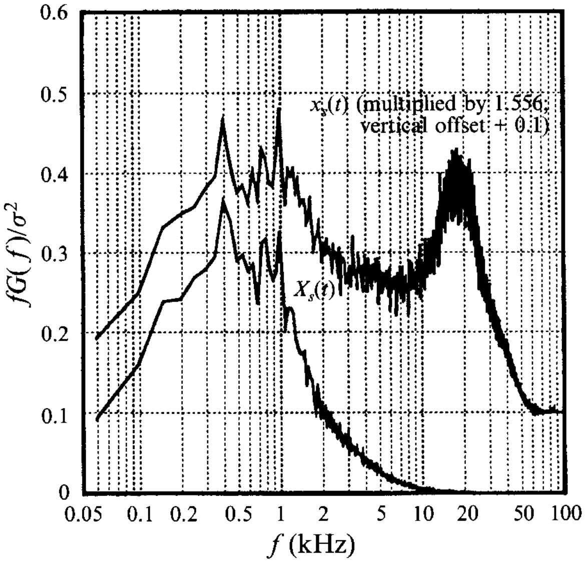

FIGURE 19. $X_S(t)$, $x_S(t)$ power spectra.

respectively, based on an $\bar{x}_S(t) \pm 3\sigma_{x_S(t)}$ variation. An improved result would probably be obtained by having the intermittent-region pressure transducers span the entire intermittent region for a more accurate calibration so that extrapolation does not occur (however, this can be difficult for large interactions).

Power spectra of $X_S(t)$ and $x_S(t)$ are shown in figure 19 (upstream sweep case; the downstream sweep case is essentially the same). As seen, the $X_S(t)$ spectrum is low-frequency dominated, whereas the $x_S(t)$ spectrum exists up to the 50 kHz analog filter limit. The most striking feature is the similarity of the two results for frequencies below about 2 kHz. In fact, the well-defined peak at about 400 Hz for $X_S(t)$ is also seen for $x_S(t)$; the additional $X_S(t)$ peaks at about 750 Hz and 1 kHz are predicted as well. Beyond 2 kHz the $x_S(t)$ result exhibits a significant amount of energy in the 10 to 30 kHz range (using Simpson's method for numerical integration, this range accounts for about 17% of the total energy in the signal; the portion below 2 kHz contains about 60%). The striking similarities at low frequency between the $X_S(t)$ and $x_S(t)$ spectra confirms that the $x_S(t)$ prediction procedure has succeeded in reproducing the low-frequency component of the separation shock foot motion and that the $\mathscr{P}_i$ distribution is a physically meaningful model for explaining the low-frequency (less than 2 kHz) component of the fluctuating wall pressures. This can even be seen in figure 18, where the low-frequency component of $x_S(t)$ does essentially match $X_S(t)$. The $x_S(t)$ prediction of a high-frequency band of energy is somewhat of an enigma. At present no direct measurements of the high-frequency motion of the shock foot are available for comparison with the $x_S(t)$ result. As a consequence, it is not known if the energy band is a true representation of shock foot motion or stems from some other source such as incoming undisturbed flow fluctuations being detected by the separated-region transducers as the separated shear layer passes above and becomes manifested in $x_S(t)$ as a high-frequency shock foot motion. This is probably the case since the 10 to 30 kHz energy band in figure 19 matches very closely with the 10 to 30 kHz energy band (most likely associated with turbulence phenomena) in the power spectra from station $-9.5\,\xi$ (figure 10*b*). As seen, even the low-frequency energy band below about 4 kHz is clearly evident in both power spectra. This further illustrates that $\mathscr{P}_i$ is the source of the low-frequency energy component measured at station $-9.5\,\xi$.

6. Brief comments on practical implications of results

6.1. *Computational fluid dynamics*

Figure 20 shows the mean wall-pressure distribution (compared with the experiments of Dolling *et al.* 1979 and Dolling & Bogdonoff 1982) and particle paths in the plane of symmetry from the Mach 3 blunt-fin computation by Hung & Buning (1985). The mean wall-pressure distribution, for $\delta/D = 1.0$, agrees well with the experimental data (for $\delta/D = 0.26$, not shown, the agreement is not as good, but reasonable overall). The inset shows the peak near the root for $\delta/D = 0.26$, which agrees with the results presented in this paper (for which δ/D is close to 1). In particular, this root peak value was seen in the ensemble average result of curves 6, figure 9 (see also the $\mathscr{P}_i$ sketch of figure 14*a*). The particle paths ($\delta/D = 1.0$) show a primary horseshoe vortex about $1.5D$ in length with its core about $0.2D$ above the surface, as well as a small secondary vortex at the fin root. The pressure minimum for $x > -1.5D$ is associated with a reversed high-speed flow zone attributed to an 'image or so-called ground effect of the vortex.' In terms of the experimental and computational results the effect of flow unsteadiness on the horseshoe vortex can now be inferred. In particular, the shape of the $\mathscr{P}_i$ distribution (the minimum) is due to the vortex ground effect, as established by the instantaneous vortex shape. When the shock foot moves upstream, the pressure levels under the vortex decrease (see figures 13 and 14*a*), indicating either that the vortex core moves toward the wall and/or that the vortex increases in strength (vice versa for downstream motion). In addition, the width of the pressure minimum increases (primarily in the upstream direction), indicating that either the vortex core moves upstream as well, or that the presence of the vortex core is sensed even further upstream, or both. Thus, as the separation shock foot moves upstream and downstream, the vortex expands and contracts, resulting in the observed low-frequency wall-pressure variations.

It appears then, that the role of the fin geometry is as follows: first, the fin geometry establishes the 'steady' flowfield character (horseshoe vortex) which gives rise to a

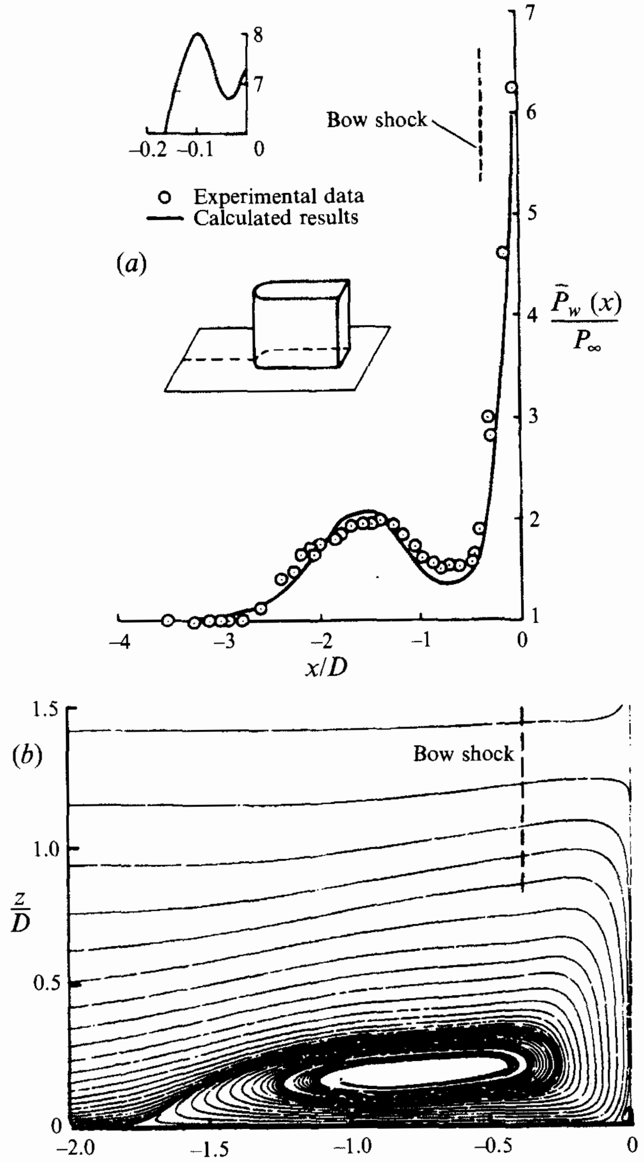

FIGURE 20. (*a*) Mach 3 computed mean pressure distribution; (*b*) particle paths in plane of symmetry (from Hung & Buning 1985).

given $\mathscr{P}_i$ distribution; then, the addition of turbulence is manifested as an unsteady flowfield in which the vortex oscillates aperiodically. A valid question is whether the vortex responds to the turbulence and consequently drives the flow, or whether the separation shock foot is driven by the turbulence and the vortex responds to the shock foot motion. The cross-correlations between the intermittent region and separated flow region support the former, as does the recent work of Erengil & Dolling (1993*b*).

As seen, the computation predicted a single mean result, although it is now clear that local pressure fluctuations are actually due to a time-dependent $\mathscr{P}_i$ distribution. The question then is, does the computational solution ($\bar{P}_w(x)$, figure 20*a*) correspond to a particular $\mathscr{P}_i$ distribution? If true, then could a series of $\mathscr{P}_i$ distributions be *calculated* by solving for the flowfield with different incoming boundary conditions such that the separation shock foot was fixed at several stations spanning the intermittent region? From these, it would be theoretically possible to estimate loading levels (or at least determine where the maximum values would occur) as was done in obtaining the $|\Delta P|$ distribution of figure 15. All that would be needed for such calculations would be correlations of UI and S locations. This method would represent a first-order inclusion of the flowfield unsteadiness into computations.

To illustrate this idea the computation shown in figure 20(*a*) for $\delta/D = 1$ (which was taken directly from Hung & Buning 1985) has been digitized and is shown replotted in figure 21(*a*). In both the computation and the experiments additional tests were made with the same incoming flow conditions, but with a thinner boundary layer. The measured and computed wall pressures are shown in figure 21(*b*). There is again good agreement between computation and experiment. As seen, by decreasing the boundary-layer thickness, the upstream influence location has been shifted downstream by about $0.3D$ (see figures 21*a* and 21*b*). Since this lengthscale change is typical of the shock foot displacement in a given flow, these two data sets offer an opportunity to make a qualitative assessment of the ideas outlined above. The pressure distribution of figure 21(*b*) is assumed to be the ensemble-averaged $\mathscr{P}_i$ distribution which would occur for the conditions of figure 21(*a*) with the shock foot at the downstream end of the intermittent region. The pressure distribution in figure 21(*a*) is assumed to be the $\mathscr{P}_i$ distribution which occurs with the shock foot at the upstream end of the intermittent region. Figure 21(*c*) shows the $|\Delta P|$ distribution obtained from the two digitized computational results and figure 21(*d*) shows the measured standard deviation distribution. The computational result (figure 21*c*) predicts three maximum values, near $-2.5D$, $-1.5D$, and $-0.25D$, and minimum values near $-2D$ and at about $-0.5D$ to $-1D$. (Note that the distribution does not extend beyond $-2.5D$ since the experimental data shown in Hung & Buning 1985 cover the data from the computation.) These agree qualitatively with the three maximum values in figure 21(*d*) near $-2.5D$, $-1.25D$, and $-0.25D$, as well as the minimum values near $-2D$ and $-0.5D$. This example once more brings out the fact that the shape of the standard deviation distribution is due to displacement of a $\mathscr{P}_i$ distribution. In addition to the computational result, figure 21(*c*) also shows the $|\Delta P|$ distribution obtained from the experimental data of figures 21(*a*) and 21(*b*). This $|\Delta P|$ distribution also has three maximum values which occur at about $-2.25D$, $-1.25D$, and $-0.25D$, as well as minimum values at about $-2D$ and $-0.5D$. The distribution does quite well in predicting the fluctuating pressure load distribution in terms of shape as well as magnitude, even though it is based on mean measurements alone.

The $|\Delta P|$ distributions of figure 21(*c*) (which were obtained from the computations and experiments) illustrate the concept and re-emphasize the possibility of using either computations or simple mean wall-pressure measurements alone in order to obtain qualitative estimates of fluctuating pressure load distributions. The accuracy of the estimates will be a function of the scale of the flowfield unsteadiness. In an experimental program for which a large variety of model geometries are available for fluctuating pressure measurements, the utility of the simplified approach becomes clear. In particular, the mean pressure distributions for all model geometries (for different boundary-layer thicknesses) could be obtained, providing standard deviation distribution estimates for all cases. From these estimates the best candidates for intensive instantaneous measurements could be selected, thereby reducing the cost of the program.

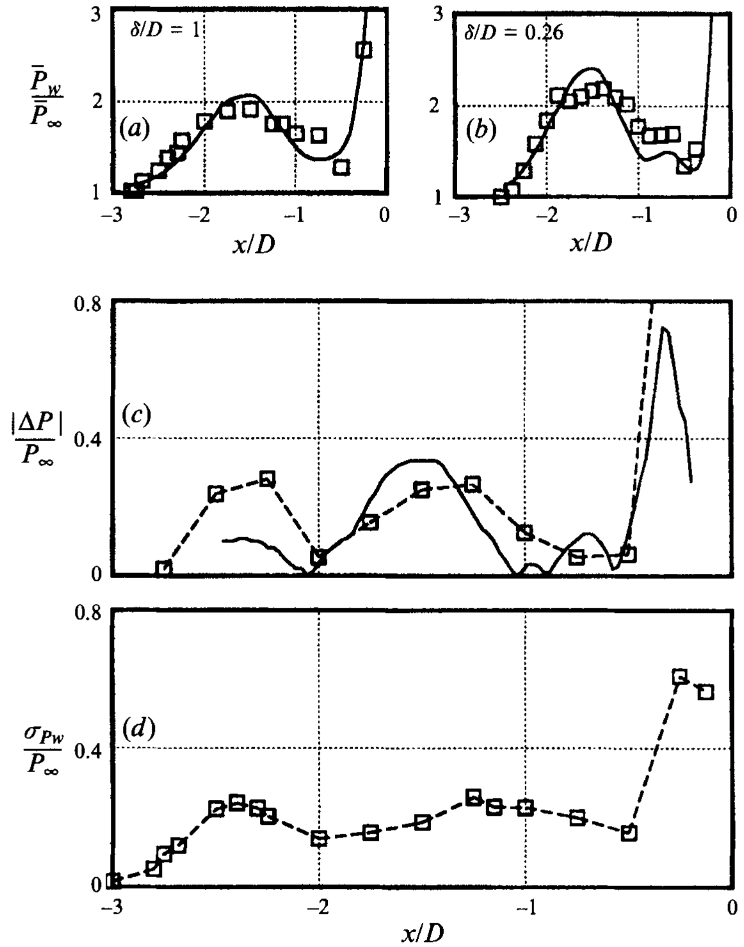

FIGURE 21. (*a*) Mean pressure distributions, $\delta/D = 1$; (*b*) mean pressure distributions, $\delta/D = 0.26$; (*c*) $|\Delta P|$ distributions; (*d*) standard deviation distribution, $\delta/D = 1$. □, Data from experiment, ——, data from computation (Hung & Buning 1985).

6.2. *Flow control*

It was shown earlier that maxima (and minima) in the centreline standard deviation distribution are due to the pressure difference $|\Delta P|$ resulting from displacements of $\mathscr{P}_i$. Therefore, in order to reduce the amplitude of local fluctuations the local $|\Delta P|$ variation, which occurs at low frequency, needs to be minimized. At this stage it does not appear that altering the high-frequency content in the flowfield would be productive. Since $\mathscr{P}_i$ is significantly affected by the primary horseshoe vortex, it may be possible to alter the large-scale low-frequency fluctuations by manipulating this vortex through model geometry changes which reduce the magnitude of the $\mathscr{P}_i$ gradient ($\partial \mathscr{P}_i / \partial x$). Since $\mathscr{P}_i$ and the mean pressure distribution have similar shapes, measurements of $\bar{P}_w(x)$ alone may be sufficient to judge the effectiveness of a given method, as discussed above.

7. Summary and conclusions

Fluctuating wall-pressure measurements have been made on the centreline upstream of a blunt fin in a Mach 5 turbulent boundary layer. Experiments were made in which a reference transducer was located under the undisturbed incoming turbulent boundary layer and simultaneous measurements were made at successive locations downstream of this station (analysis A). Analyses B and C were essentially the same as analysis A, but the reference transducer was located at different stations in the intermittent region. Cross-correlation results from these analyses demonstrated that a correlation does exist between each of the three flowfield regions. The cross-correlation results showed the existence of two modes, a broad mode associated with the low-frequency content of the signals, and a sharp mode associated with high frequencies. 'Transition' points in the flowfield were identified based on changes in character of the broad mode in the cross-correlations. Ensemble averages of the B and C test series showed the existence of two characteristic signatures, a broad (low-frequency) signature and a sharp (high-frequency) signature. For analysis A, digital filtering demonstrated that frequencies below 4 kHz contribute to the low frequency (broad mode) in the cross-correlation, and also that the ensemble averages contain low-frequency contributions which were not obvious in the unfiltered result.

By examining the ensemble-averaged wall-pressure distributions for different shock-foot-fixed positions, it has been shown that local fluctuating wall-pressure measurements are due to a distinct pressure distribution, $\mathscr{P}_i$, which undergoes a stretching and flattening effect as its upstream boundary translates aperiodically between the upstream-influence and separation lines. The locations of the maxima and minima in the centreline wall-pressure standard deviation distribution were accurately predicted using this distribution, providing quantitative confirmation of the model. A qualitative discussion of the local wall-pressure measurements which would be obtained if $\mathscr{P}_i$ were shifted upstream or downstream, analogous to upstream and downstream sweeps of the shock foot, agreed with the observed character of the ensemble averages. Further, by a qualitative examination of the type of cross-correlations which would be obtained from certain model signals, and by then comparing the ensemble-average results to the model signals, the source of the broad mode in the cross-correlations (i.e. $\mathscr{P}_i$) was qualitatively verified. Thus, the low-frequency content of the pressure signals from downstream of the shock foot are due to the $\mathscr{P}_i$ distribution. The high-frequency content of the signals, in particular the sharp mode of the cross-correlations and the sharp signature in the ensemble averages, are due to convection of the incoming undisturbed boundary-layer flow into and through the interaction.

Strong quantitative support for the $\mathscr{P}_i$ model was provided when wall-pressure signals from under the separated-flow region were used to predict the position–time history of the separation shock foot. The low-frequency content (less than about 2 kHz) of the predicted shock foot position–time history, $x_S(t)$, matched extremely well with the measured shock foot position–time history, $X_S(t)$. The analysis also predicted a shock motion in the 10 to 30 kHz range which could not be confirmed, since no measurements of separation shock foot motion for frequencies greater than about 2 kHz are available for comparison with $x_S(t)$.

From these results, a detailed physical explanation of the measurements and correlations in Dolling & Brusniak (1991) has been provided. Finally, the unsteady flowfield can be described as follows. The fin geometry establishes the 'steady' flowfield character, namely the horseshoe vortex (and secondary root vortex) which gives rise to the 'steady' $\mathscr{P}_i$ distribution. With turbulence the flowfield becomes unsteady. In particular, as the foot of the separation shock moves upstream and downstream the leading edge of the vortex also moves upstream and downstream, and the vortex expands and contracts, so that the centreline pressure variations are due to a time-varying $\mathscr{P}_i$ distribution which undergoes distortion and aperiodic motion. The results have the following implications. First, by computing mean wall-pressure distributions for several shock-foot-fixed cases (in conjunction with shock foot lengthscale correlations and intermittency distributions) or by using mean wall-pressure distributions from experiments, it may be possible to predict some of the unsteady aspects of shock wave/turbulent boundary layer interaction separated flowfields. Second, in order to minimize the fluctuating loads caused by the flow unsteadiness, methods should focus on reducing the magnitude of the $\mathscr{P}_i$ gradient $(\partial\mathscr{P}_i/\partial x)$.

This work was supported by NASA Lewis under Grant NAG3-1023 monitored by Warren Hingst. This source of support is gratefully acknowledged. The manuscript was typeset by Jeanie Duvall. Her expertise and many helpful suggestions are gratefully acknowledged.

REFERENCES

Bendat, J. D. & Piersol, A. G. 1986 *Random Data, Analysis and Measurement Procedures*, 2nd edition. John Wiley.

Brusniak, L. 1994 Physics of unsteady blunt fin-induced shock wave/turbulent boundary layer interactions. PhD dissertation, Dept of Aerospace Engineering & Engineering Mechanics, The University of Texas at Austin.

Dolling, D. S. 1993 Fluctuating loads in shock wave/turbulent boundary layer interaction: tutorial and update. *AIAA Paper* 93-0284.

Dolling, D. S. & Bogdonoff, S. M. 1981*a* Scaling of interactions of cylinders with supersonic turbulent boundary layers. *AIAA J.* **19**, 655–657.

Dolling, D. S. & Bogdonoff, S. M. 1981*b* An experimental investigation of the unsteady behavior of blunt fin-induced shock wave turbulent boundary layer interactions. *AIAA Paper* 81-1287.

Dolling, D. S. & Bogdonoff, S. M. 1982 Blunt fin-induced shock wave/turbulent boundary layer interaction. *AIAA J.* **20**, 1674–1680.

Dolling, D. S. & Brusniak, L. 1989 Separation shock motion in fin, cylinder, and compression ramp-induced turbulent interactions. *AIAA J.* **27**, 734–742.

Dolling, D. S. & Brusniak, L. 1991 Correlation of separation shock motion in a cylinder-induced interaction with pressure fluctuations under the separated region. *AIAA Paper* 91-0650.

Dolling, D. S., Cosad, C. D. & Bogdonoff, S. M. 1979 An examination of blunt fin-induced shock wave turbulent boundary layer interaction. *AIAA Paper* 79-0068.

Dolling, D. S. & Smith, D. R. 1989 Separation shock dynamics in Mach 5 turbulent interactions induced by cylinders. *AIAA J.* **27**, 1698–1706.

Erengil, M. E. & Dolling, D. S. 1993*a* Effects of sweepback on unsteady separation in Mach 5 compression ramp interactions. *AIAA J.* **31**, 302–311.

Erengil, M. E. & Dolling, D. S. 1993*b* Physical causes of separation shock unsteadiness in shock wave/turbulent boundary-layer interactions. *AIAA Paper* 93-3134.

Gonsalez, J. C. & Dolling, D. S. 1993 Correlation of interaction sweepback effects on the dynamics of shock-induced turbulent separation. *AIAA Paper* 93-0776.

Gramann, R. A. & Dolling, D. S. 1988 Detection of turbulent boundary layer separation using fluctuating wall pressure signals. *AIAA Paper* 88-4676.

Holden, M. S. 1986 A review of aerothermal problems associated with hypersonic flight. *AIAA Paper* 86-0267.

Hung, C.-M. & Buning, P. E. 1985 Simulation of blunt-fin-induced shock-wave and turbulent boundary-layer interaction. *J. Fluid Mech.* **154**, 163–185.

KLEIFGES, K. & DOLLING, D. S. 1993 Control of unsteady shock-induced turbulent boundary layer separation upstream of blunt fins. *AIAA Paper* 93-3281.

KUSSOY, M. I., BROWN, J. D., BROWN, J. L., LOCKMAN, W. K. & HORSTMAN, C. C. 1987 Fluctuations and massive separation in three-dimensional shock-wave/boundary-layer interactions. *2nd Int. Symp. on Transport Phenomena in Turbulent Flows, Tokyo, Japan, Oct. 25–29.*

LAKSHMANAN, B. & TIWARI, S. N. 1993 Study of supersonic intersection flowfield at modified wing-body junctions. *AIAA J.* **31**, 877–883.

MCCLURE, W. B. 1992 An experimental study of the driving mechanism and control of the unsteady shock-induced turbulent separation in a Mach 5 compression corner flow. PhD dissertation, Dept of Aerospace Engineering & Engineering Mechanics, The University of Texas at Austin.

NARLO, J. C. 1986 Experimental investigation of the driving mechanisms of separation shock wave motion in interactive flows. MS thesis, Dept of Aerospace Engineering & Engineering Mechanics, The University of Texas at Austin.

POZEFSKY, P., BLEVINS, R. D. & LAGANELLI, A. L. 1989 Thermo-vibro-acoustic loads and fatigue of hypersonic flight vehicle structures. *AFWAL* TR-89-3014.

SUN, C.-C. & CHILDS, M. E. 1973 A modified wall-wake velocity profile for turbulent compressible boundary layers. *J. Aircraft* **10**, 381–383.